FTA: A Feature Tracking Empirical Model of Auroral Precipitation

Chen Wu[1], Aaron Ridley[1], Anna DeJong[2,3], Larry Paxton[4]

[1]Climate and Space Sciences and Engineering, University of Michigan, Ann Arbor, Michigan, USA

[2]Department of Physics, Catholic University of America, Washington, District of Columbia, USA

[3]NASA Goddard Space Flight Center, Greenbelt, Maryland, USA

[4]Applied Physics Laboratory, Johns Hopkins University, Laurel, Maryland, USA

Key Points:

- The AE-based FTA Model provides the energy flux and the average energy using 1.5 years of Polar Ultraviolet Imager data.
- The FTA model's grid is tied to auroral boundaries and spatial distribution: tracking a cumulative energy grid in each MLT sector.
- For the March 17, 2013 event, the FTA model had the most confined patterns and agreed best with SSUSI observations of auroral power.

Corresponding author: Chen Wu, `chenwum@umich.edu`

Abstract

The Feature Tracking of Aurora (FTA) Model was constructed using 1.5 years of Polar Ultraviolet Imager data and is based on tracking a cumulative energy grid in 96 magnetic local time (MLT) sectors. The equatorward boundary, poleward boundary, and 19 cumulative energy bins are tracked with the energy flux and the latitudinal position. With AE increasing, the equatorward boundary moves to lower latitudes everywhere, while the poleward boundary moves poleward in the 2300-0300 MLT region and equatorward in other MLT sectors. This results in the aurora getting wider on the nightside and becoming narrower on the dayside. The peak intensity of the aurora in each MLT sector is almost linearly related to AE, with the global peak moving from pre-midnight to post-midnight as geomagnetic activity increases. Ratios between the Lyman-Birge-Hopfield-long and -short models allow the average energy to be calculated. Predictions from the FTA and two other auroral models were compared to the measurements by the Defense Meteorological Satellite Program Special Sensor Ultraviolet Spectrographic Imagers (SSUSI) on 17 March 2013. Among the three models, the FTA model specified the most confined patterns with the highest energy flux, agreeing with the spatial and temporal evolution of SSUSI measurements better and predicted auroral power (AP) better during higher activity levels (SSUSI AP > 20 GW). The Fuller-Rowell and Evans (1987) and FTA models specified very similar average energy compared with SSUSI measurements, doing slightly better by ∼1 keV than the OVATION Prime model.

1 Introduction

The aurora is induced by collisions between precipitating energetic electrons or ions and the atmosphere. These precipitating particles are accelerated by or diffused from different regions of the magnetosphere and act as a window into dynamical processes of the solar wind-magnetosphere-ionosphere system. The aurora is highly dynamic both spatially and temporally, especially under geomagnetically active conditions. On a large scale, the auroral oval is the footprint of magnetospheric boundaries, which experience great changes in shape and location (Feldstein, 1973; Akasofu, 1966; Milan, 2009; Milan et al., 2009, etc). Within the aurora, meso-scale (with scale sizes of 10s to 100s of kilometers) to small-scale (with spatial scales down to tens of meters and temporal scales down to fractions of a second) structures appear as arcs, spots, patches, etc. of visual emissions with different luminosities and behaviors, most of which represent complex energy

–2–

transport between magnetosphere and ionosphere (Maggs & Davis, 1968; Borovsky et al., 1991; Frey, 2007; Sandahl et al., 2008; Paschmann et al., 2012; Forsyth et al., 2020; Nishimura et al., 2020, etc.). The energy flow and structure within the auroral oval are therefore complicated and dynamic under different geomagnetic conditions.

Recent observational studies have shown that the upward field-aligned currents (FACs) coincide with the aurora both spatially and temporally (e.g., Murphy et al., 2013; Carter et al., 2016). Murphy et al. (2013) demonstrated that the upward FAC elements of the structured substorm current wedge were spatially correlated with discrete aurora during the substorm expansion phase and that discrete changes in the FAC topology were observed in the late growth phase before auroral substorm expansion phase onset. Statistical comparisons between simultaneous observations by the constellation of Iridium satellites and the Global Ultraviolet Imager (GUVI), performed by Korth et al. (2014), found that the electron precipitation inferred from the auroral emission occurred primarily within and near the large-scale upward current regions under southward interplanetary magnetic field (IMF) conditions, while the correlation was smaller for northward IMF, presumably due to the lack of enough statistical events. Also, the correspondence was evident at dusk where a larger fraction of the electron precipitation is accelerated downward by a field-aligned potential difference. However, it was uncorrelated from pre-midnight through dawn to noon, consistent with diffuse electron precipitation dominating the incident energy flux. Korth et al. (2004) examined FACs observed by the Iridium constellation for 25 events of prolonged steady northward IMF and found that the occurrence of high-latitude dayside aurora is generally restricted to solar wind proton densities below 4 cm^{-3} and peak current densities higher than 0.7 $\mu A\ m^{-2}$ under all observed solar wind conditions. Carter et al. (2016) found that the FACs and auroral oval move to lower latitudes as the IMF becomes both increasingly stronger in magnitude and increasingly southward. However, the lack of coincidence between the R1 FAC and the auroral oval in the dusk sector is contrary to expectation, since the discrete electron aurora on the duskside was thought to be associated with the R1 FAC and thus the downward precipitating electrons (e.g., Elphic et al., 1998; Newell et al., 2009; Korth et al., 2014).

For both understanding and simulating the high-latitude thermosphere-ionosphere system, auroral precipitation is a dominant source of energy and needs to be well specified. In addition, auroral precipitation drives ionization, which controls the electron and ion

densities, leading to composition, momentum, and energy exchange between the ionosphere and thermosphere. The auroral precipitation therefore plays a crucial role in the dynamics of the winds, heating, and composition of the upper atmosphere. Great efforts have been made to establish various auroral precipitation models based on both images and particle measurements organized by geomagnetic indices like Kp (Hardy et al., 1985; Zhang & Paxton, 2008), SuperMAG auroral electrojet (Mitchell et al., 2013), and solar wind (Brautigam et al., 1991; Newell et al., 2010a, 2014). See Newell et al. (2015) for a review of different methods of constructing auroral precipitation models. Traditionally, these empirical precipitation models bin data based on a latitude grid in fixed geomagnetic coordinates. This smooths the latitudinal distribution, since the auroral oval is highly dynamic in location, size, and latitudinal energy structure, as described above, especially during higher magnetospheric activity. To overcome this smoothing issue, previous studies about the high-latitude ionospheric electrodynamics have binned the convection/potential (Heppner & Maynard, 1987; Rich & Hairston, 1994; Weimer, 2005; Chisham, 2017; Zhu et al., 2020), the particle precipitation (e.g., Sotirelis & Newell, 2000; Redmon et al., 2010; Zhu et al., 2020), subauroral polarization (Landry & Anderson, 2018), FACs (Kilcommons et al., 2017), etc. in dynamic coordinates, which were basically with a "boundary-oriented" binning approach, though the reference boundaries and latitudinal bins varied.

Sotirelis and Newell (2000), based on measurements by the Defense Meteorological Satellite Project (DMSP) satellites, presented a global configuration of electrons precipitating from 32 eV to 30 keV, ordering precipitation relative to 5 auroral boundaries on the nightside and 3 on the dayside. They concluded that the resulting model more closely resembles instantaneous observations. Redmon et al. (2010) devised an algorithm to identify the aurora regions using precipitation electron observations from the DMSP Special Sensor Version 4 (SSJ4) based on a figure of merit and then mapped the observations to its fractional position within the auroral zone or polar cap referring to the boundaries. This method was improved by Kilcommons et al. (2017) utilizing coincident data from the DMSP precipitating electrons and ions instrument (SSJ5). To investigate the differences between the static and the "boundary-oriented" binning approaches, Zhu et al. (2020) binned the electron precipitation data from DMSP SSJ5 with both methods for moderately strong and dominantly southward IMF conditions. They concluded that

–4–

the "boundary-oriented" binning approach provided a more confined and intense electron precipitation pattern.

In this study, a new auroral electron precipitation model is presented. This model uses an adaptive coordinate system, like the works discussed above. However, instead of using latitude bins (as Sotirelis and Newell (2000), Redmon et al. (2010), and Zhu et al. (2020) do), the Feature Tracking of the Aurora (FTA) Model uses cumulative energy bins as a latitudinal coordinate. The FTA model is keyed off of the AE index, which captures the dynamics of the auroral state, and was produced using data from Polar Ultraviolet Imager (UVI) N_2 Lyman-Birge-Hopfield-long (LBHl) and -short (LBHs) emission images between 1 January 1997, and 30 June 1998. This study presents initial results from this model as well as a comparison of three precipitation models and measurements by the Special Sensor Ultraviolet Spectrographic Imagers (SSUSIs) on the DMSP satellites on 17 March 2013.

2 Methodology

2.1 Data Used to Create the FTA Model

The UVI instrument onboard the Polar spacecraft started operation in 1996, providing imagery of the global aurora in 4 far ultraviolet (FUV) filters covering spectral regions from 130 nm to 190 nm for at least 9 hours of the 18-hour elliptical orbit. Images were integrated over about 37 s and had an angular resolution of $0.036°$ (Torr et al., 1995). The characteristics of the precipitation can be obtained from emissions in N_2 LBH bands. The energy flux can be inferred from the LBHl emissions, while the average energy can be calculated from the ratio of the LBHl to the LHBs (Strickland et al., 1983; Germany et al., 1994; Brittnacher et al., 1997). In this study, the auroral brightness in LBHl was converted to the energy flux with the proportionality constant of $110\ R/(erg\ cm^{-2}\ s^{-1})$ (Germany et al., 1994; Brittnacher et al., 1997). The average energy was derived based on the relationship with the emission ratio indicated by Germany et al. (1994). Each LBHl or LBHs image was processed by first removing the dayglow and then following the procedure described below.

The AE index utilized to organize the image measurements was extracted from NASA/GSFC's OMNI data set through OMNIWeb with 1-min resolution.

–5–

2.2 Background Subtraction and Boundary Identification

Several approaches of determining the boundaries from auroral images have been described previously, including simple methods that involve using a constant threshold of auroral brightness (Frank & Craven, 1988; Brittnacher et al., 1999) and a fixed ratio to the maximum of the auroral oval within a local time slice (Kauristie et al., 1999; Baker et al., 2000). More complex approaches considered the spatial information to segment the auroral oval, such as the neural network-based method (Germany et al., 1998), the clustering-based method (Wang et al., 2011; Ding et al., 2017), and functional fitting of the global auroral oval (Carbary et al., 2003; Ding et al., 2017). In this study, when the aurora was weak, the boundaries were identified using a constant threshold of 110 R, as was done in previous studies (e.g., Brittnacher et al., 1999; Carbary, 2005; Baker et al., 2000). However, with increasing activity, the noise of the background exceeded 110 R, so that a fixed threshold was not appropriate (Baker et al., 2000). Therefore, for intense aurora, the k-means clustering algorithm (Hartigan & Wong, 1979) was applied in the determination of the equatorward boundary (EB) and the poleward boundary (PB).

The k-means clustering method classified the emissions into several groups in which each data point belonged to the group with the nearest mean, i.e., the auroral image was clustered into different intensity levels. For intense aurora, the k-means clustering method differentiated the oval from the background. Visually, with 8 clusters of increasing intensity levels, the background of the emission was included in groups 0 and 1. The training set contained two components: the brightness and the magnetic latitude (MLat). Figure 1a shows an example of an image of the UVI/LBHl emission from the northern hemisphere at 11:48:06 UT on 23 June 1997, with the dayglow-removal and smoothing processes applied. Some of the background was larger than 110 R. Using the k-means clustering algorithm, the image was clustered into different intensity levels, as shown in Figure 1b. The background (groups 0 and 1) was distinct from the auroral oval. Thus the group 1-group 2 boundary then set the equatorward and poleward edge locations of the oval. The luminosities in groups 2 and above were typically larger than 110 R for intense aurora, but for lower activity times, they usually included brightnesses lower than this value (not shown here) and then the threshold 110 R was utilized to determine the boundaries.
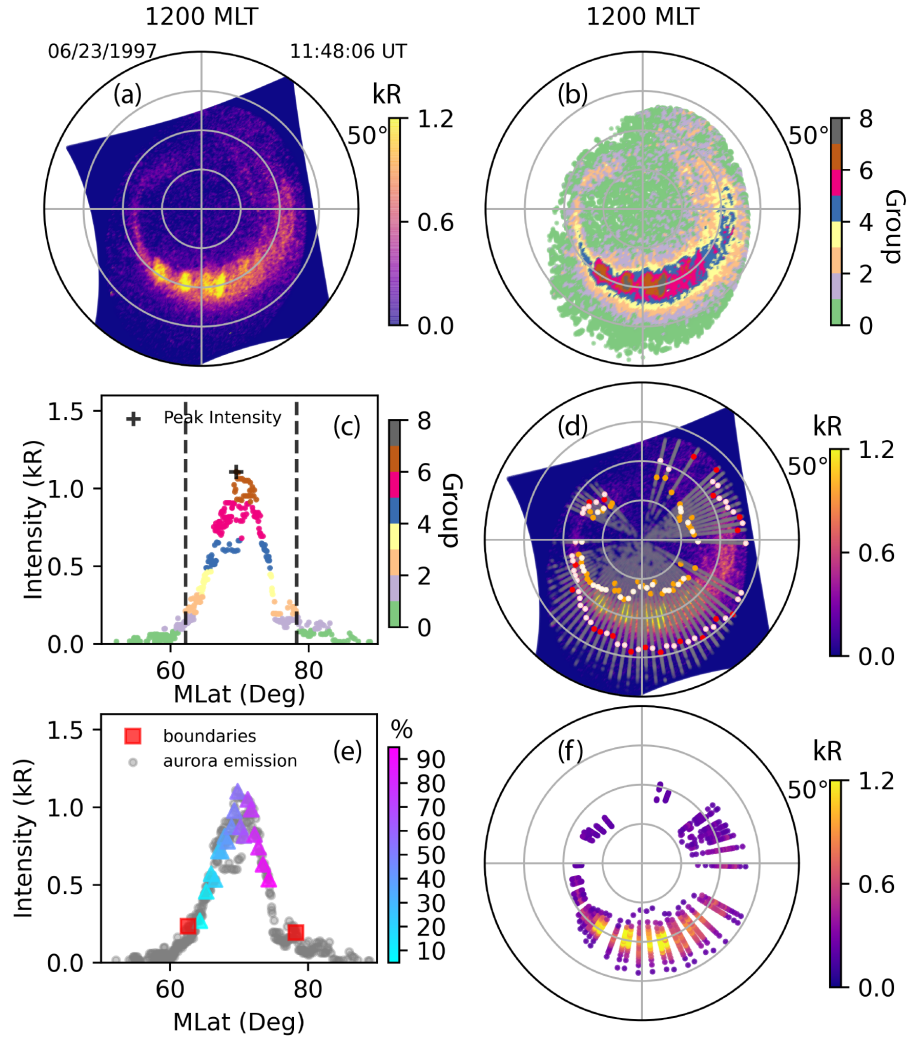
Figure 1. An example of dealing with one image. (a) the result after dayglow-removal and smoothing; (b) k-means clustering method applied to the image; (c) in 0000-0015 MLT sector, the grouped emission data as a function of MLat and the boundaries marked by the two black dashed lines; (d) boundaries of the auroral oval in each MLT bin. The grey lines represent the medians of the MLT bins, and the white, red, and orange dots together denote the boundaries determined, and the red and orange are data far away from their neighbors; (e) the 19 levels of the cumulative energy (blue to magenta triangles) and the auroral boundaries (red squares) in 0000-0015 MLT sector; (f) the auroral oval reconstructed with the brightness and the location in the valid MLT bins and the 21 cumulative energy bins. The AE index was 257 nT. All the dial plots are in MLat and MLT coordinates with noon (1200 MLT) at the top and dusk (1800 MLT) at the left. The MLat range is from 50° to 90° and the grey circles represent MLat at 80°, 70°, and 60°.

173 For each auroral image, the data was binned in $\frac{1}{4}$ h magnetic local time (MLT) bins

174 (0000-0015 MLT, 0015-0030 MLT, ..., 2345-2400 MLT) for a total of 96 bins. Figure 1c

175 presents the EB and PB (two dashed lines) identified in the MLT bin of 0000-0015 MLT.

176 The emission data belonged to k-means clustering 7 groups. Figure 1d shows boundaries

177 of the auroral oval in each MLT bin. Some MLT bins were discarded for a variety of

178 reasons, including: (1) the cutoff of the field of view was falsely identified as the EB; (2)

179 the auroral width was too small (< 21 points, less than $\sim 2°$ in latitude); and (3) the

180 location of the determined EB varied too much from its four nearest neighbors. In the

181 second situation, the aurora was usually very weak. The gaps on the dayside occurred

182 where the MLT bins were discarded due to weak intensity or small width, while those on

183 the dawnside were due to the cutoff of the field of view, which was too close to the auroral

184 oval. At points where the color is red or orange, the latitude of the boundary in that MLT

185 bin fell more than one standard deviation outside of the four neighbors. In general, the

186 EB location varied relatively smoothly as a function of MLT. However, when the auroral

187 intensity was perturbed (see the nightside MLT bins) or the aurora was too weak to be

188 distinguished from the background (see the dayside MLT bins), it was identified too far

189 away from its neighbors. Unlike the EB, the PBs latitudinal location was more dynamic

190 and irregular with a larger uncertainty. The PB outside of the one standard deviation of

191 its neighbors would be set to a null value, but would not be used to determine whether

192 the MLT bin was discarded or not. Note that these conditions were designed to be

193 conservative and exclude non-auroral observations as much as possible. Future work will

194 include more weak intensities and perturbations of the aurora in the model by loosening

195 these restrictions.

196 The sources of error in the boundary locations can come from the k-means method

197 throwing away data (groups 0 and 1). To estimate a possible uncertainty on the location

198 of the EB, if the aurora constructed by the FTA model was projected down to the 110 R

199 level at the boundary (for AE=300, MLT=0300), then the EB would be about $1°$ lower

200 latitude (total width of the aurora for these conditions was about $9.5°$), but that is well

201 within the $\sim 3°$ standard deviation. As another validation of the boundary selection

202 technique, the ratio of the intensity at the PB to the peak intensity for each MLT bin was

203 calculated and compared with results by Baker et al. (2000). In Figure 2, for different

204 MLT regions (0000-0600 MLT, 0600-1200 MLT, 1200-1800 MLT, and 1800-2400 MLT),

205 the median and interquartile values of the ratio are shown as a function of AE. The ratios

–8–

were higher for lower activity and roughly stayed constant for AE larger than 200 nT. Using the same data source, Baker et al. (2000) used a ratio threshold of 0.3 between the boundary and peak intensity. In Figure 2, on the nightside for the FTA model, the ratio was about 0.25 with the interquartile range of ∼0.1-0.15. On the dayside the ratio was ∼0.45 in the morning sector and ∼0.4 in the afternoon sector, due to the fact the peak brightness was lower. Therefore, the k-means method (throwing out groups 0 and 1) possibly gives an error, but it is consistent with other studies, and the error is less than the variability in the equatorward edge location. It may therefore be better to try to determine the cause of the variability than to come up with a better way of eliminating the background noise.

After processing, the numbers of the LBHl and LBHs images were 114,970 and 116,058 in total. Figure 3 shows the distribution of the EB and PB events in each AE/MLT bin for the LBHl emission measurements. For AE lower than 500 nT, both the EB and PB had above ∼100 counts in each MLT/AE bin and above ∼700 counts in each grid on the nightside. As activity increases, the points in each grid become less than 100 on the dayside, and when AE was above 900 nT, the PB event dropped below 100 at dawn. The data distribution for the LBHs images is similar (not shown).

2.3 Cumulative Energy Binning

For each LBHl/ LBHs image, in each MLT sector, the aurora was binned using cumulative energy bins. The emission data in each independent MLT sector was integrated latitudinally from the EB to the PB, resulting in a total intensity cumulative distribution function. Then 19 levels (5%, 10%, 15%, ..., 95%), as well as the boundaries (i.e., the EB and PB, respectively), were sampled as 21 grid points to track intensity and latitude. For example, in Figure 1e, for the MLT bin of 0000-0015 MLT, the 21 grid points (the auroral boundaries and the 19 levels) are shown. Figure 1f shows the auroral oval reconstructed with the brightness and the location in the valid MLT bins and the 21 cumulative energy bins. This was then the information that was used to develop the FTA model.

The cumulative energy distribution ranged from 0-100% and could be scaled in latitude easily, therefore it was considered to be a good feature to track with a built-in grid system. Because the data was sampled based on the energy distribution, the brightest

–9–
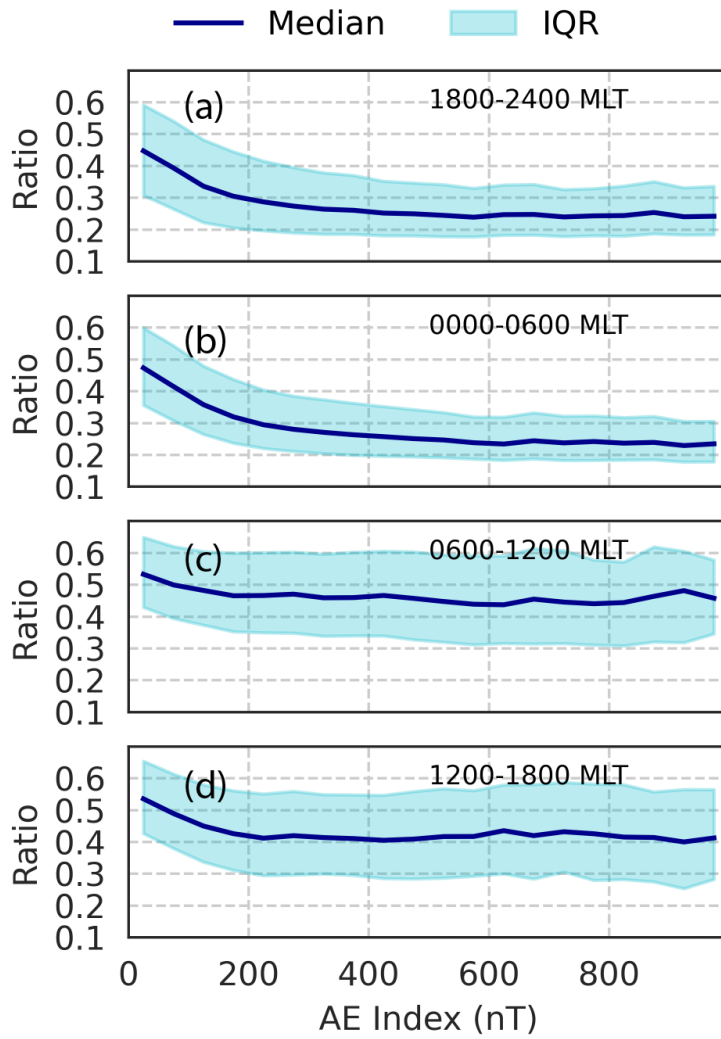
Figure 2. The median and interquartile values of the ratio of the intensity at the poleward boundary to the peak intensity in each MLT bin for different MLT sectors.
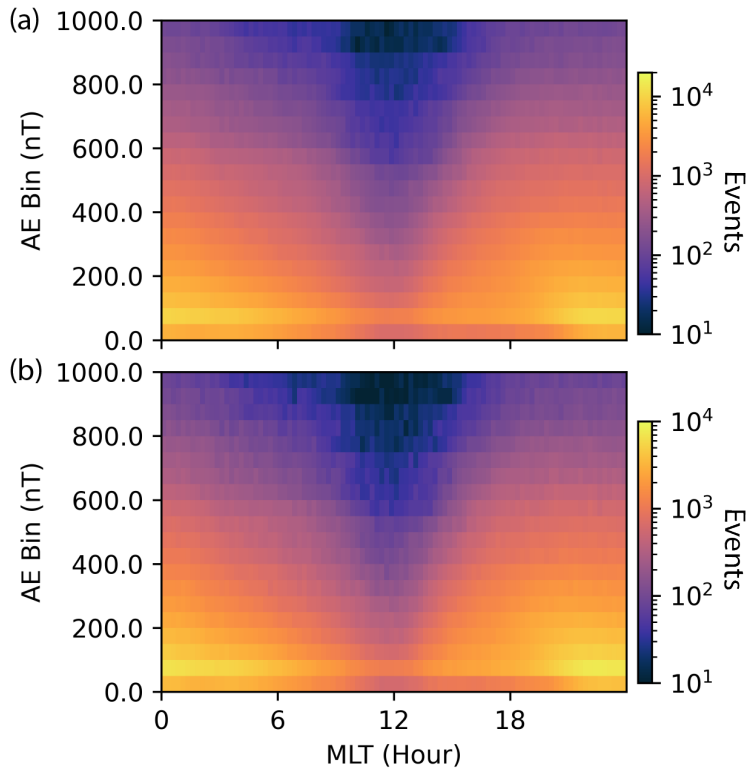
Figure 3. Distribution of EB (a) and PB (b) events in each AE/MLT bin for the LBHl emission. The AE bins are from 0 to 1000 nT with an interval of 50 nT. For EB, the maximum count is 11,014 (AE: 50-100 nT, 2215-2230 MLT) and the minimum count is 8 (AE: 900-950 nT, 1000-1015 MLT); for PB, the maximum count is 7,521 (AE: 50-100 nT, 2215-2230 MLT) and the minimum count is 5 (AE: 900-950 nT, 1200-1215 MLT).

emission region contributed more to the cumulative energy and therefore was sampled at finer resolution. As shown in Figure 1e, more data were selected near the EB than at the PB where the auroral emission was weaker. Consequently, while the Sotirelis and Newell (2000) model presented appropriate sharp transitions of different regions, including the polar cap, due to more sophisticated boundaries, the FTA model with the cumulative energy binning method should be able to better capture the intense auroral emissions adaptively. In addition, since the Sotirelis and Newell (2000) model was based on 5 boundaries on the nightside and 3 boundaries on the dayside, which resulted in the discontinuity between the dayside and the nightside, and the DMSP measurements used in the model had poor coverage in the post-noon and post-midnight regions, from a global perspective, the FTA model based on auroral images by Polar UVI with the cumulative energy bins should be more zonally consistent.

3 FTA Model

After binning each series of LBHl/LBHs images in the 96 MLT bins and the 21 cumulative energy bins, the data was organized by the AE index from 0 to 1000 nT with an interval of 50 nT. For each AE bin, 96×21 pairs of averaged brightness and MLat were obtained. With the average MLat information in each AE bin, the global emission could be projected to the MLT/MLat coordinates. The energy flux (Figure 4) and the average energy (Figure 5) were then calculated based on the LBHl and LBHs emissions for each AE bin.

Compared to the traditional MLT/MLat binning method, the energy flux of the FTA model has the following characteristics:

1. The auroral morphology of the FTA model looks thinner than traditional models: the width of the energy flux pattern is less than $11°$ with AE smaller than 450 nT and does not exceed $14°$ when the geomagnetic activity becomes high. When the AE index is ~450 nT, the corresponding Kp index is roughly from 1.5 to 5 (Rostoker, 1991). Under this condition, the width of the energy flux pattern exceeds ~$15°$ in the Fuller-Rowell and Evans (1987) (FRE) model and the Zhang and Paxton (2008) model. In the study by Zhu et al. (2020), it was found that the "boundary-oriented" method reduced the auroral width by about 50% on the duskside compared to the static binning approach.

–12–
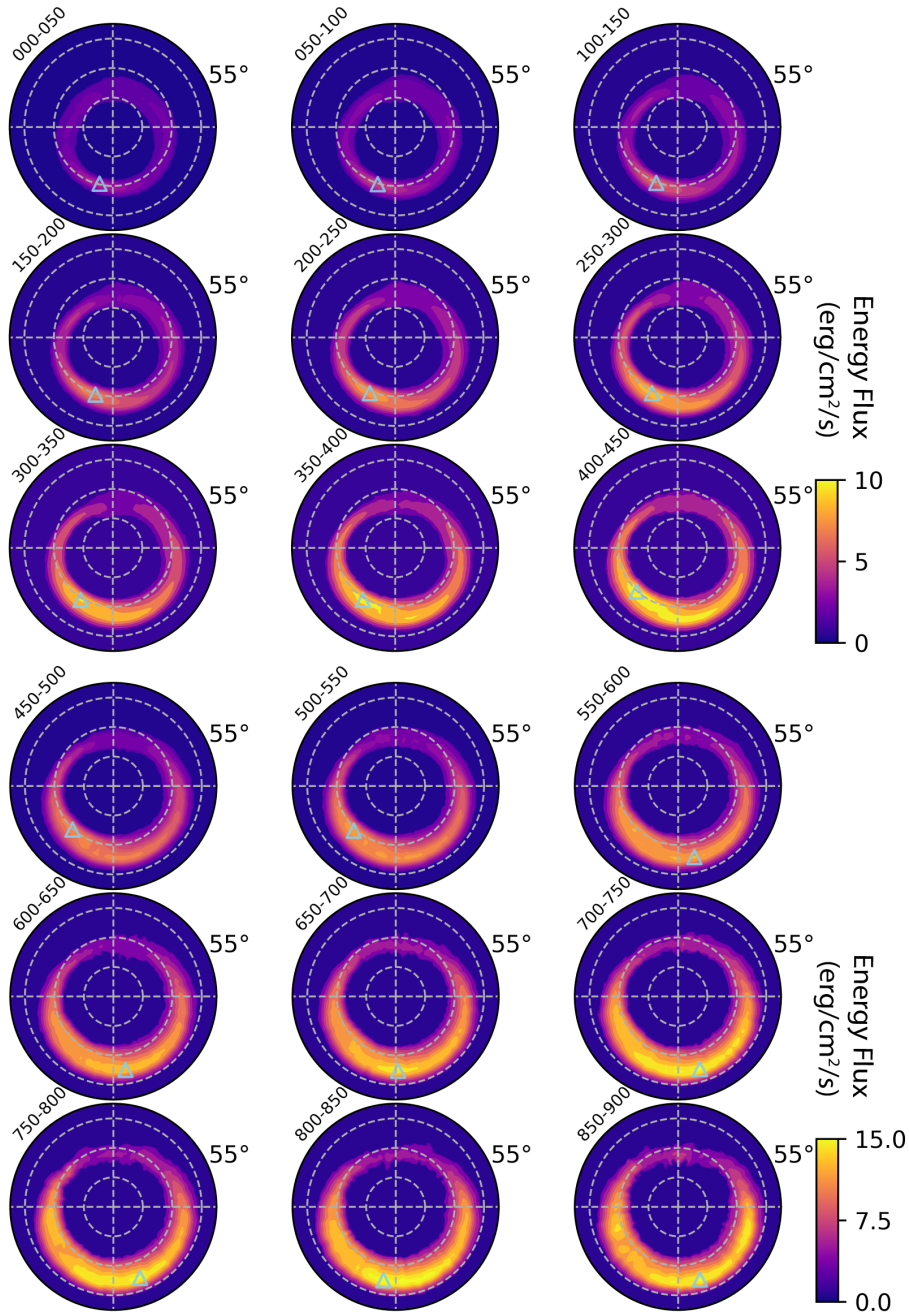
Figure 4. Patterns of the energy flux. The AE bin (unit: nT) was labeled on the upper left increasing from the left to the right and from the top to the bottom. Note that different color scales were applied with AE index larger and smaller than 450 nT. The triangle denotes the location of the global maximum of the energy flux. All the dial plots are in MLat and MLT coordinates with noon (1200 MLT) at the top and dusk (1800 MLT) at the left. The MLat range is from 55° to 90° and the white dashed circles represent MLat at 80°, 70°, and 60°.

2. The FTA model presents a different dawn-dusk asymmetry. Current models, like the FRE model and the Zhang and Paxton (2008) model, described the energy flux on the dawn side being higher than that on the duskside under weak and moderate magnetic activity, while as the activity increases, it was roughly symmetric in the dawn-dusk direction. The FTA model is consistent with these models during quiet times. However, with AE from 200 nT to 450 nT, the aurora from post-noon through pre-midnight becomes intense and has a larger energy flux than the dawnside, which indicates opposite dawn-dusk asymmetry to the models mentioned above. Based on the comparison of the static and the "boundary-oriented" binning methods for the moderately strong IMF, Zhu et al. (2020) found that the enhancements of the energy flux are more substantial in the 1400-2400 MLT sector than those in 0200-1200 MLT sector for the dynamic binning pattern with the peak magnitude in the 1400-2400 MLT sector exceeding 50% of that in the static binning results. This is consistent with the present results. As known, the dusk to pre-midnight sector is relatively active: it is dominated by monoenergetic aurora and the substorm onsets (e.g., Akasofu, 1966; Newell et al., 2009). Therefore, this different dawn-dusk asymmetry may be explained by better capturing of the intense and dynamic auroral features due to the new binning method.

3. Fine features are revealed as the aurora evolves with AE. The FTA model presents typical features at various activity levels, which are consistent with previous studies (e.g., Lui et al., 1989; Liou et al., 1997, 2001; Luan et al., 2018) and other precipitation models (e.g., Fuller-Rowell & Evans, 1987; Sotirelis & Newell, 2000; Zhang & Paxton, 2008). However, more details seem to be revealed in this study. As known, the aurora should follow upward FACs, which means that there should be a step change in the location of the aurora across midnight, with pre-midnight being poleward of post-midnight. This can be qualitatively observed in the FTA model at AE of 350-450 nT, as a relatively rapid change in contour location across midnight. In the quantitative analysis sector below, it is described in more detail.

Different magnetospheric modes may be indicated in the FTA model. At lower activity levels (AE $<\sim$ 400 nT), the peak is in the pre-midnight sector, while at higher activity levels, the aurora becomes broader in MLT and the peak moves to midnight or post-midnight. This is consistent with the transition from isolated substorms to storm-time substorms or sawtooth events (Pytte et al., 1978; Henderson, 2004; DeJong et

–14–

al., 2009; DeJong et al., 2018; Cai & Clauer, 2013; Walach et al., 2017). However, different modes cannot be distinguished from each other clearly in the FTA model, because the data has not been divided by the type of magnetospheric mode. Further work is needed to determine the dependencies of the aurora on different drivers, which may be possible to parameterize using AU, AL, and Dst.

Figure 5 presents the average energy within the FTA model. The average energy is larger on the equatorward edge of the oval on the dawnside through pre-noon, while it is enhanced closer to the poleward edge on the duskside through post-noon. The pattern is consistent with the average energy pattern by Sotirelis and Newell (2000) and Fuller-Rowell and Evans (1987). For higher activity, an intensified region occurs across the nightside located at the equatorward of the enhancement in the pre-midnight sector and consistent with the latitudinal location of the enhancement in the post-midnight sector. This variation seems to agree with that of the characteristic energy in Fuller-Rowell and Evans (1987).

4 Results

Since the LBHl emission is proportional to the energy flux, the auroral boundaries (EB and PB locations) and the peak intensity (magnitude and latitudinal location) of the LBHl emission in each MLT bin are investigated in this section. The hemispheric power (HP) of the FTA model is also presented.

4.1 Boundary Movement

To investigate the motion of the boundaries as activity increases, for each MLT bin, the mean locations of EB and PB were plotted as a function of AE. The boundary locations vary almost linearly with AE up to 800 nT. The change in boundary location shows a strong dependence on MLT: the EB shifts to lower latitudes at different rates, while the direction of the PB movement can be equatorward or poleward as activity increases. To investigate further, linear least-squares fittings were calculated between the raw data and the AE index for each MLT bin. The slopes of the fitted lines, i.e., the change in MLat per 50 nT AE bin as a function of MLT, are shown in Figure 7a. The slope of the EB shows that it moves to lower latitudes at a faster rate on the nightside with a value of $-0.38 \sim -0.51°/\text{AE}$ (50 nT) bin and has a slower rate close to noon. Two peaks occur

–15–
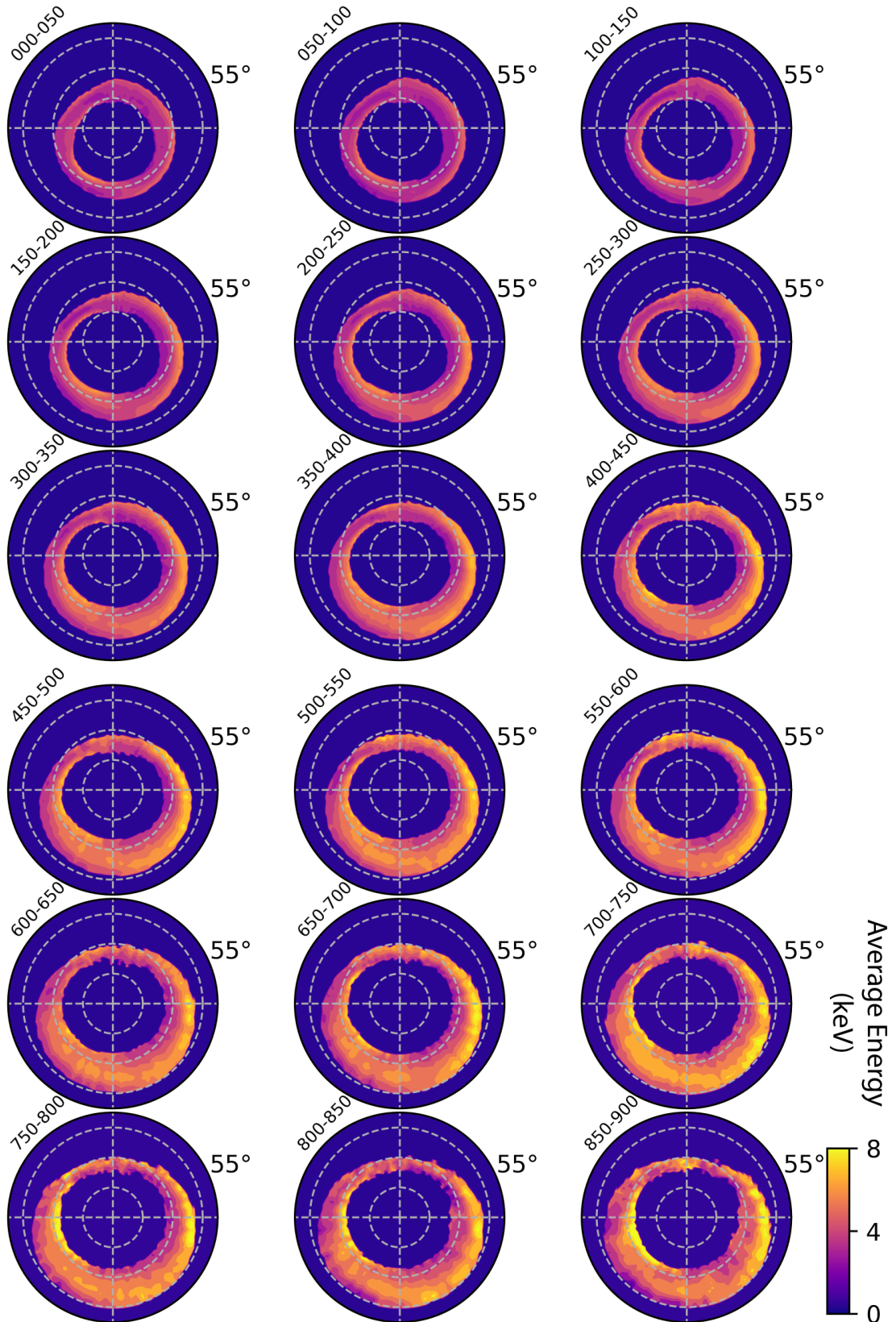
Figure 5. Similar to Figure 4, but for the average energy.
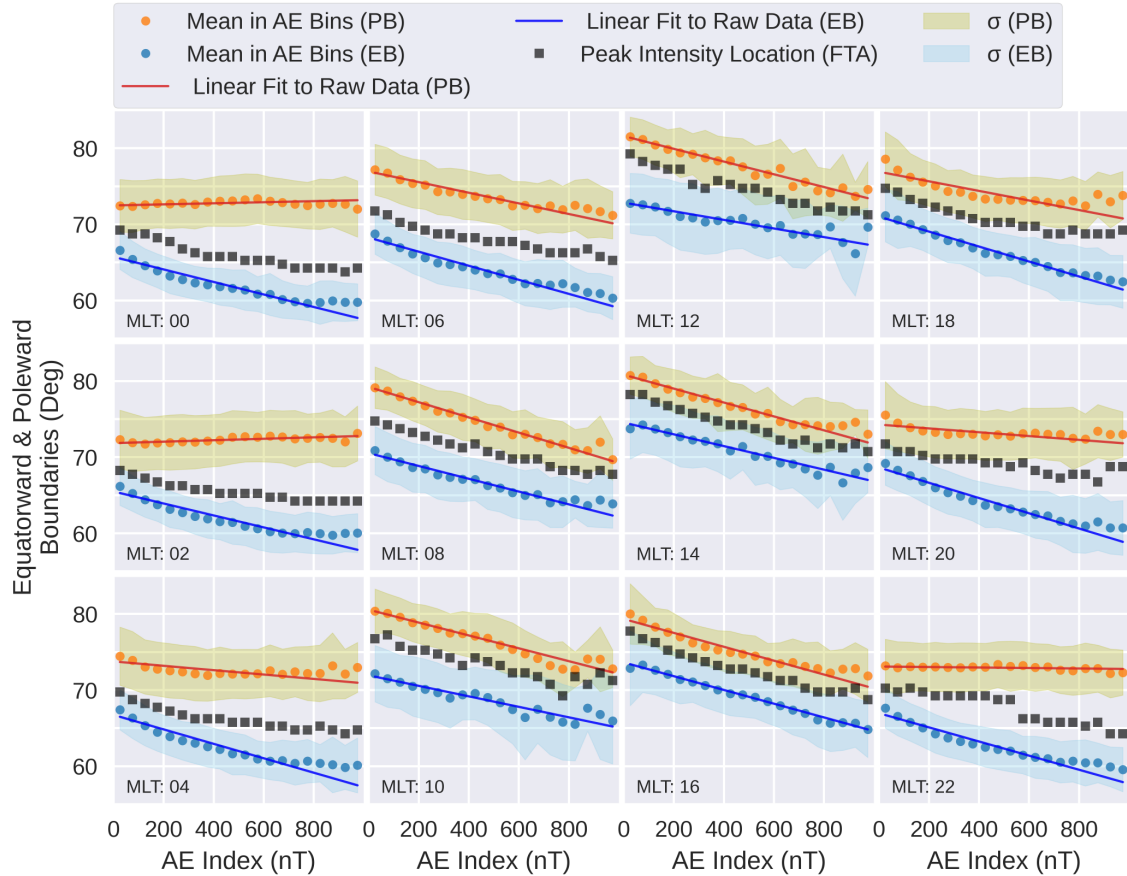
Figure 6. Mean of the EB and PB locations in each AE bin as a function of AE for twelve MLT bins (every other hour). The light blue (EB) and olive (PB) shaded regions represent one standard deviation (σ) in each MLT bin. The dark blue (EB) and dark red (PB) lines represent the linear fittings between the raw data and the AE index in each MLT bin. The black square represents the peak intensity location derived from the FTA model for each MLT/AE bin.

before sunrise and after sunset with the values of -0.48°/ 50 nT and -0.51°/ 50 nT, while a minimum of -0.26°/ 50 nT occurs around noon. The PB, on the other hand, moves equatorward faster than the EB in most sectors on the dayside with two peaks of -0.5°/ 50 nT around 0800 MLT and 1500 MLT, then becomes slower and slower towards midnight, ceases at ∼0300 MLT and ∼2300 MLT, and moves poleward with a peak of 0.06°/ 50 nT at ∼0200 MLT. The width of the auroral oval (PB location minus EB location), consequently increases on the nightside, decreases on the dayside, and remains the same in the transmission zone between the two (roughly post-dawn and pre-dusk, denoted by dashed lines).
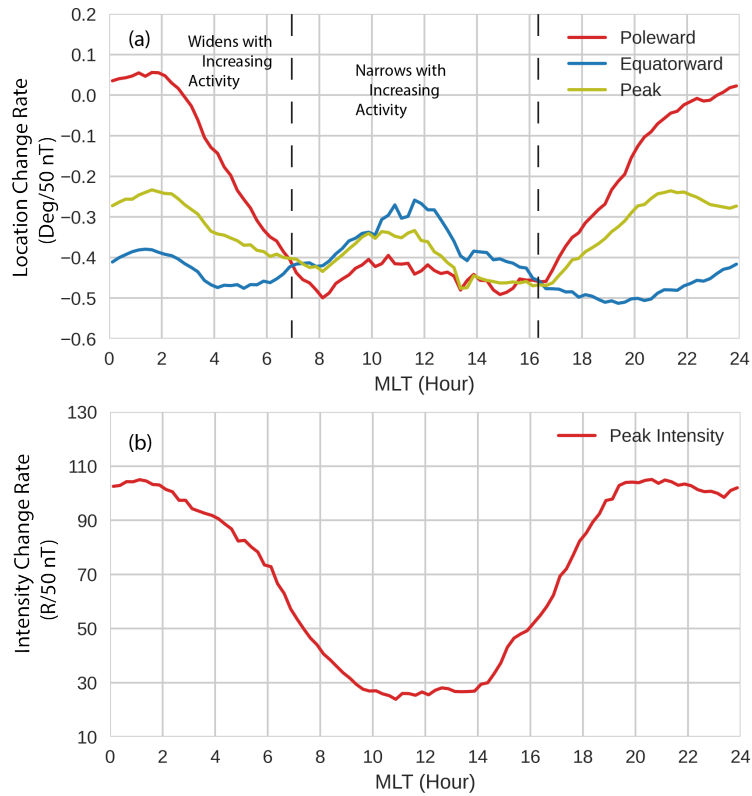
Figure 7. (a) For EB, PB, and the peak intensity location, the change in magnetic latitude per 50 nT AE bin as a function of MLT. The dashed lines represent the MLTs where the rate of change for EB equals that for PB. (b) The change of peak intensity per 50 nT AE bin as a function of MLT.

340   These results are generally consistent with but show different details from other studies.

341   For example, based on 4 months of Polar UVI measurements, Carbary (2005) constructed

342   a simple model of the auroral boundaries organized by Kp. They found linear

343   relationships between the boundaries and the geomagnetic activity, which failed at higher

344   activity levels, consistent with the conclusions in this study. However, the previous study

345   indicated that with activity increasing, the EB moved to lower latitudes at a faster rate in

346   the post-noon sector, while the PB moved equatorward in the post-noon sector and

347   poleward on the entire nightside statistically, which is different from the results here.

348   Recently, Mooney et al. (2020) studied the open-closed field line boundary (OCB)

349   movement during substorms based on IMAGE FUV images. It was found that within ∼10

350   min of the beginning of the substorms, in the MLT prior to the onset MLT sectors (MLT

351   difference approximately from -4 to -1 h), the OCB moved equatorward due to the

352   increasing open flux during the growth phase, while in the MLT sectors near and after the

353   onset MLT (MLT differences from 0 to 4 h), the OCB tended to contract poleward or

354   showed no changes in the latitude location. This is consistent with the PB movements in

355   Figure 7a. As shown, the PB stays in a fixed latitude at ∼2300 MLT where the substorm

356   onsets mostly occur, while it moves equatorward in earlier MLT sectors and poleward in

357   later MLT sectors. However, for a longer time after the substorm onsets, in the MLT

358   region within ±3 h from the onset sectors that were determined by locations of the center

359   of the sudden brightness at the beginning of the expansion phase and had MLT

360   distribution peaking at ∼23 MLT and MLat distribution peaking at ∼ 66° (Liou et al.,

361   2001; Frey et al., 2004), the OCB moved poleward, and the statistical movement of PB in

362   this study does not agree with it. This may indicate a need to differentiate between

363   substorm expansion phase (i.e., AE increasing) and recovery phase (i.e., AE decreasing).

364   Figure 6 shows that, when the geomagnetic activity becomes high enough (i.e., AE > 800

365   nT), the aurora does not move to lower latitudes at the linear rate. This could be a result

366   of a saturation effect or the lack of enough statistical data at high activity levels. It is

367   difficult to determine the reason for this behavior without more data. Due to this

368   limitation, the FTA model was not extrapolated with linear fits beyond the geomagnetic

369   activity range of 0-1000 nT, which covers roughly 99.18% of the time.

4.2 Peak Intensity of the Emission

Figure 1c shows an example of the peak identified in one MLT sector, denoted as a cross. The magnitude and location of the peak intensity for each MLT bin were investigated with the same approach applied for the EB and the PB. As shown in Figure 8a, the peak intensity increases with AE. The rate of change in the magnitude, which is represented by the slope of the fitted line, was calculated and is shown in Figure 7b, while the rate of the change in the location was over-plotted in Figure 7a so that it can be compared with the auroral oval boundary motion rates. The rate of the intensity change (Figure 7b) shows a diurnal pattern with the peak on the nightside of ∼105 R/50 nT and the trough of ∼26 R/50 nT at noon. An asymmetry between dusk and dawn exists, with dusk aurora increasing at a faster rate than dawn. As indicated by the rate of change in the location (Figure 7a), the peak moves to lower latitudes slower than the EB on the nightside and faster than the EB on the dayside as geomagnetic activity increases. In addition, a dawn-dusk asymmetry is observed in the motion of the peak location of the oval, with the 1600-1800 MLT sector moving equatorward faster than the 0600-0800 MLT sector, consistent with the EB.

The peak intensity for each MLT bin as a function of AE was plotted in Figure 8b. The intensity increases with AE at different rates for different MLT sectors. In general, it increases linearly for lower AEs and tends to saturate for higher AEs with the nightside rate of increase greater than the dayside as indicated above. In addition, at lower activity levels, the maximum of the peaks occurs pre-midnight, but switches to post-midnight at around 500 nT, which is consistent with the global peak intensity denoted by the blue triangle in Figure 4. The latitudinal location of the peak intensity of the 21 cumulative energy bins in each MLT bin was over-plotted in Figure 6. The change of the MLat is approximate 5° equatorward with AE increasing from 0 to 1000 nT both in the pre- and post-midnight sectors. However, there is a slight difference between the two regions. In the post-midnight region (0200-0400 MLT), the peak moves equatorward faster as AE increases and then stays at the same latitudes for AE larger than 500-600 nT, while the motion in the pre-midnight (2000-2200 MLT) is relatively slower at lower AE levels, but the peak keeps moving to lower latitude for AE larger than 600 nT. This may be associated with the "FAC-like" structures described in Figure 4, indicating that the difference of the latitudinal locations of the peak in the pre- and post-midnight regions becomes larger and then smaller as AE increases. The similar asymmetric aurora pattern
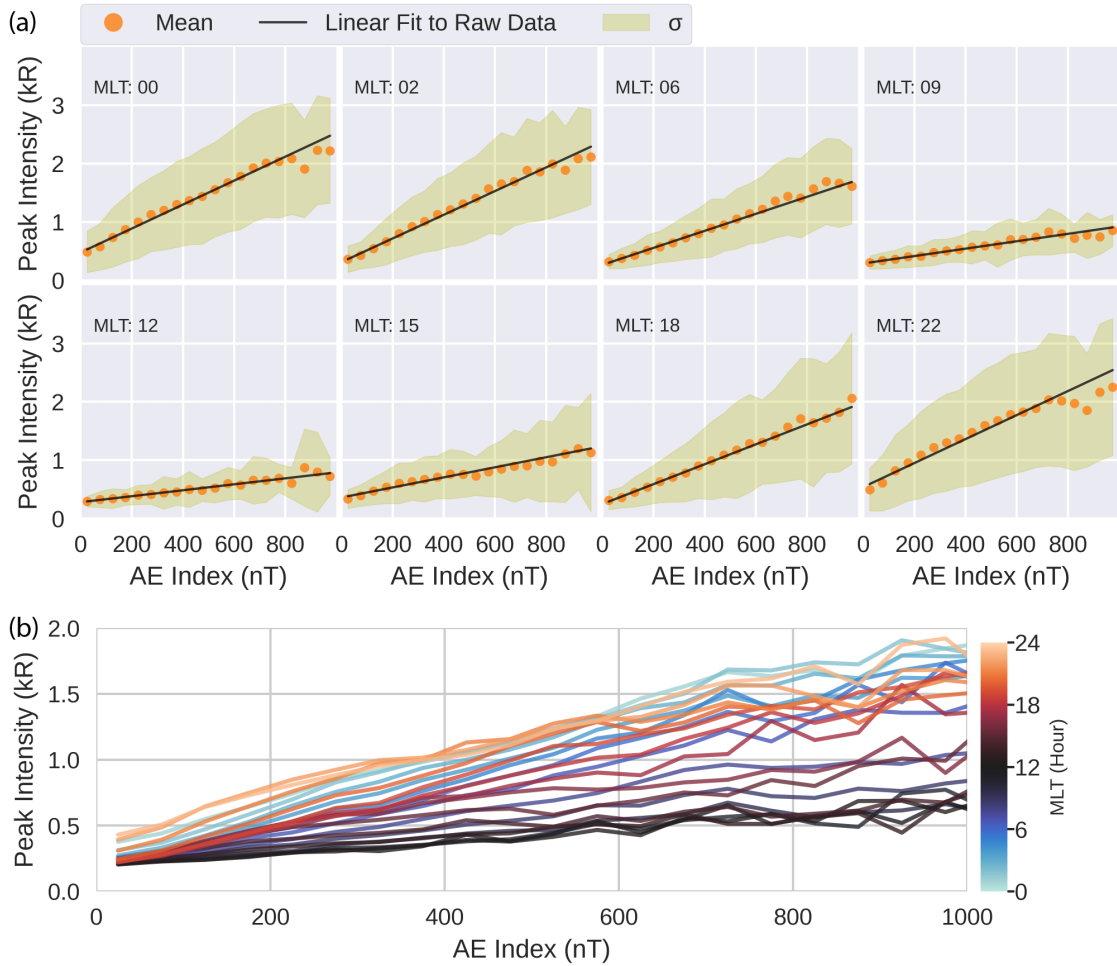
Figure 8. (a) Similar to Figure 6, but for the peak intensity and only eight MLT bins are shown to save space; (b) the peak intensity derived from the FTA model for different MLT bins as a function of AE.

was reported by Korth et al. (2014). They compared the statistical distributions of the large-scale Birkeland currents from the Iridium constellation with a composite distribution of simultaneously obtained electron precipitation inferred from the auroral images by GUVI and found that for southward IMF, the electron precipitation occurs primarily within and near the upward current regions. This implied that the asymmetric pattern of the aurora near midnight is likely to be associated with upward currents, which are a part of the higher latitude, R1 current system on the dusk (pre-midnight) side and a part of the lower-latitude, R2 current system on the dawn (post-midnight) side. For the AE of 300-500 nT, the nightside data points exceed 1000 for each MLT/cumulative-energy/AE bin, indicating that it has good data coverage and probably is a significant feature. However, the possibility that it is contributed from the uneven data coverage or insufficient smoothing cannot be excluded and needs further study.

4.3 Hemispheric Power

The HP is the rate of the total energy deposition integrated over the northern/southern auroral zone and thus can be applied in the configuration of energy inputs of ionospheric and thermospheric models and can serve as an indicator of the large-scale predictive capability of auroral precipitation models (Zhang & Paxton, 2008; Newell et al., 2010b; Newell et al., 2014). Figure 9a shows the FTA model HP as a function of the AE index. Note the energy flux was integrated on the dayside, the nightside, and the entire northern hemisphere, respectively, so that the auroral power over different regions could be compared. The uncertainty of the auroral power was calculated based on the standard deviation of the energy flux in each grid. As shown in Figure 9a, the HP increases almost linearly with the AE index, having a larger slope on the nightside than on the dayside, though having a possible non-linear relationship when AE becomes larger than 750 nT, which may be due to lack of enough data or a saturation effect at higher AE levels. In Figure 9b, the ratio of the nightside power to the dayside power increases from $\sim$1.3 to $\sim$3.4 when AE is smaller than 650 nT, while it stays around 3.4 after that. This indicates that under lower activity conditions, the energy deposited on the nightside increases faster than the dayside with AE increasing. However, as geomagnetic activity increases, the rate of energy input on the nightside slows down and gradually equals 3.4 times that on the dayside.
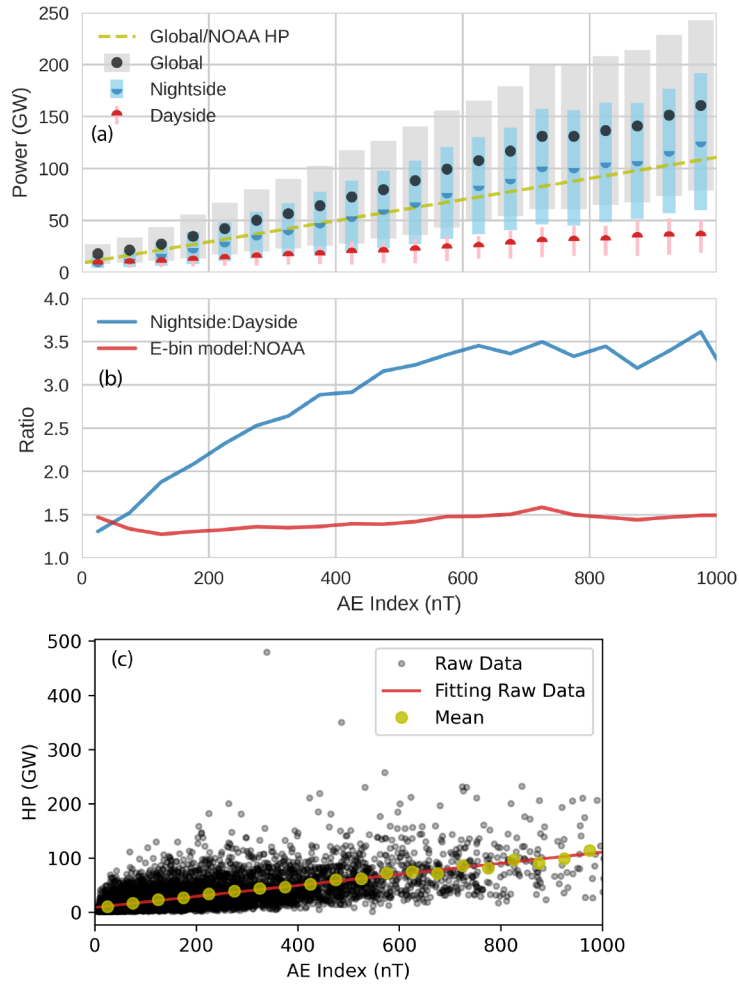
Figure 9. (a) Dayside, nightside, global HP of the FTA model, and the linear-fitting NOAA HP as a function of the AE index bin. Errorbars (the grey, blue, red are for the global, nightside, and dayside regions) are added. (b) HP ratios of the nightside aurora to the dayside aurora and the global HP of the FTA model to the linear-fitting NOAA HP, respectively. (c) The NOAA HP as a function of the AE index.

The National Oceanic and Atmospheric Administration (NOAA) HP (Emery et al., 2006, and references therein) was used to determine whether the global energy input from the FTA model was roughly correct. NOAAs Polar Orbiting Environmental Satellites system (formerly known as TIROS for Television and InfraRed Observation Satellite) continually monitored the energy flux carried by precipitating protons and electrons during every pass from 1978 through 2013, except for 1989 and 1990. With the energy flux observations during these passes, the actual total energy over a polar region was estimated based on the satellite data compared to statistical patterns of auroral energy flux for 10 levels of the auroral activity constructed from historical data (Fuller-Rowell & Evans, 1987). To get the relationship between NOAA HP and AE index, a linear least-squares fitting was applied to fit the datasets in 1997, as shown in Figure 9c. The derived equation was:

$$HP \, [GW] = 0.102 \, [GW \ nT^{-1}] \times AE \, [nT] + 8.953 \, [GW] \qquad (1)$$

Figure 9a shows Equation 1 as a yellow dashed line. The HP of the FTA model is significantly larger than the predicted NOAA HP. The ratio between the global FTA HP and the predicted NOAA HP, shown in Figure 9b, is roughly constant at around 1.5. This difference is likely due to the fact that the NOAA derivation of HP relies on the statistical patterns of the FRE model and single dawn-dusk cuts of the auroral oval. However, since the NOAA satellites use particle instruments while the FTA model is built based on image data, the offset between FTA HP and NOAA HP could also be contributed from instrumental difference: Emery et al. (2006) adjusted 28 years of HP estimated from 11 NOAA and 11 DMSP satellites and all 22 satellite adjustments were within a factor of 2. The ratio of FTA HP to NOAA HP is 1.5, indicating that the two datasets are about as consistent as other measurements.

5 Comparisons for the March 2013 Storm

5.1 Data and Models for Comparisons

The SSUSI instruments are hosted on the F16, F17, F18, and F19 of the DMSP-Block 5D3 satellites in near-polar, sun-synchronous orbits at an altitude of approximately 850 km with periods of roughly 101 min. The F19 spacecraft was launched in April 2014, and therefore only F16, F17, and F18 spacecrafts had measurements for the March 2013 storm that was investigated in this study. SSUSI records the auroral images in five FUV bands

–24–

with a cross-track spectrographic imager across the plane of the orbit as the spacecraft orbits, taking ∼20-30 min to capture the entire auroral oval in one hemisphere (Paxton et al., 1992, 1993; Paxton & Meng, 1999; Paxton et al., 2017).

Fuller-Rowell and Evans (1987) constructed statistical global patterns of Pedersen and Hall conductances for 10 discrete levels of aurora activity, established using indices generated from the energy deposited into a single hemisphere from particle observations. The model also provides the total energy flux and the average energy. Newell et al. (2010a) constructed the OVATION Prime (OP) model (consisting of four types of aurora: diffuse, monoenergetic, broadband, and ion aurora) from electron and ion flux measurements by the DMSP satellites. For each type of aurora, separate linear regression fits to the Newell coupling function (Newell et al., 2007), were applied for each MLT-MLat bin. The OP model provides the energy flux, the number flux, and the average energy for each type of aurora, which was extended to higher disturbance levels by using images from the GUVI instrument (Newell et al., 2014).

The spatial resolutions of the FRE and the OP models were $2°$ (MLat) $\times$ 0.8 h (MLT) and $0.25°$ (MLat) $\times$ 0.25 h (MLT), respectively, while the FTA model was binned with 96 MLT bins (0.25 h each) and 21 cumulative energy bins. The MLat resolution of the FTA model varied with MLT and AE. For example, on the nightside, it was less than $0.1°$ under lower activity conditions or larger than $2°$ during higher activity; the median spacing increased from $0.27°$ to $0.53°$ with higher activity. To compare the predictions of the three models and the observations from SSUSI consistently, the results of the models and the measurements were linearly interpolated to a resolution of $0.5°$ (MLat) $\times$ 0.25 h (MLT). Since SSUSI did not measure the aurora instantaneously and polar pass covered ∼20-30 min, the auroral image was segmented into 96 MLT bins and the UT at $65°$ MLat was estimated. This was done by taking the cartesian coordinate of the satellite in the dawn-dusk direction and assigning the time in which the satellite passed through the projection of the cell position at $65°$ latitude. This way, the MLT bins in which the satellite did not pass through could be visualized.

The FRE and OP models were developed with particle data, while the FTA model is based on auroral image data. Though there are differences between the measurements of auroral precipitations (e.g., Mende, 2016, and references therein), for statistical models, some large-scale characteristics of the aurora, like the auroral boundaries, the peak

–25–

intensity in each MLT sectors, and the dawn-dusk asymmetry, etc., should be comparable. Baker et al. (2000) found a systematic latitudinal offset of 1° between the DMSP b5e boundaries and the PBs that were identified by a fixed ratio to the maximum in each MLT sector from Polar UVI images in the evening sector. Zhang and Paxton (2008) indicated that the NOAA and DMSP HP were bounded by the HP estimated based on GUVI auroral images and a rough correlation among the HP was found as they tended to reach their peaks/minimums around the same time. Since this study is an introduction to the FTA model, a case comparison involving the large-scale characteristics was conducted aiming to obtain some general conclusions. More comprehensively comparative studies will be carried out in the future with more details of the aurora, analysis of instrumental difference, and more events with other magnetospheric modes, taken into consideration. For simplicity, 1.0 $erg\ cm^{-2}\ s^{-1}$ was used to locate the auroral boundaries in the three models, as well as in the SSUSI measurements. In addition, because there is low energy electron precipitation on the poleward edge of the aurora that cannot be detected by the UVI under normal circumstances, the PBs of different instrument-based models are likely to have a larger difference and are not compared in this study.

5.2 March 2013 Storm Event

On 17 March 2013, there was a geomagnetic storm that provided a good opportunity to investigate the capability of different auroral precipitation models. To make a comparison, the results calculated by the FRE, OP, and FTA models were compared to DMSP SSUSI measurements.

Figure 10 shows variations of the AE index, the IMF B_y and B_z, the solar wind velocity, the Newell coupling function ($\frac{d\Phi}{dt}$, defined by Newell et al. (2007)), and the NOAA HP on 17 March 2013. The AE index and the HP drive the FTA model and the FRE model, respectively, while $\frac{d\Phi}{dt}$, calculated from the IMF and solar wind parameters, drives the OP model. At the beginning of the day, B_y and B_z were weak, with small solar wind velocity, and $\frac{d\Phi}{dt}$ was accordingly small. The AE index and the HP were weak too. At ∼6:00 UT, the AE index started to increase rapidly, exceeding 1000 nT in a few minutes, coinciding with an increase of HP, and then AE decreased. Subsequently, there came several decreases and increases of B_z and a long-lasting negative B_z between 15:00 and 22:00 UT with an increased $\frac{d\Phi}{dt}$ due to the large velocity and southward IMF. The AE index was perturbed with most of the values above 500 nT and occasionally exceeded 1000 nT and
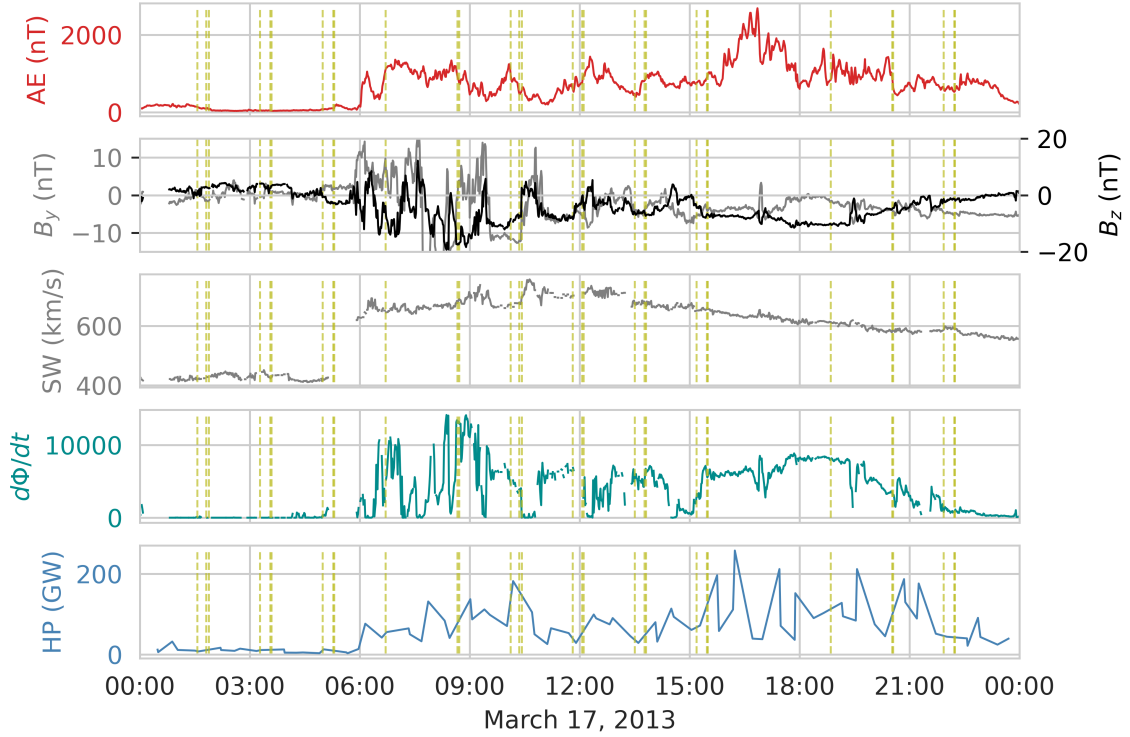
Figure 10. Variations of the AE index, the IMF-B_y, the IMF-B_z, the solar wind velocity, the rate magnetic flux is opened at the magnetopause ($\frac{d\Phi}{dt}$), and the NOAA HP. The AE index, the solar wind velocity, the IMF-B_y, and the IMF-B_z were extracted from NASA/GSFC's OMNI data set through OMNIWeb. The yellow dashed lines represent the times that were investigated.

even 2000 nT. The HP was large during this disturbed time but with more variability. In order to explore how well the FTA model performed, the 38 times indicated by the yellow dashed lines were examined. Due to poor statistical results of the FTA model during higher geomagnetic conditions, only times with AE no larger than 900 nT were compared in this study.

5.3 Energy Flux and Average Energy

Figures 11 and 12 show patterns of the energy flux and the average energy from the three models and the SSUSI measurements. The average energy for the models are shown in Figure 12 if the energy flux is larger than 1.0 $erg\ cm^{-2}\ s^{-1}$ to avoid significant noise.

–27–

Images from 6 of the 38 orbits are presented in Figures 11 and 12, including two times of lower activity and 4 times of higher activity.

The energy flux predicted by the FTA model had the most confined patterns with the highest energy flux, as expected due to the new binning approach. At lower activity, the FRE and OP models specified little aurora on the dayside and weak emissions on the dawnside, while the FTA model had intenser aurora globally with local enhancements. From the SSUSI measurements, there existed intense regions of aurora on the dayside and the duskside, agreeing more with the enhancements specified by the FTA model, except for the weak response in the morning sector at 01:48 UT. During the active time, the aurora was highly dynamic and structured. The duskside measurements by SSUSI strengthened at 10:21 UT and 15:11 UT and were relatively weak at 13:30 UT and 22:13 UT, while in the dawn and morning regions, the aurora was most enhanced at 15:11 UT. When confined to the regions corresponding to the SSUSI measurements, the FRE model predicted that the energy flux was more intense at 10:21 UT and 22:13 UT on the duskside and at 22:13 UT in the morning sector. The energy flux of the OP model was larger at 10:21 UT and 13:30 UT on the duskside and at 13:30 UT on the dawnside. Compared to the two models, the FTA model agreed more with the evolution of SSUSI energy flux temporally with enhancements at 10:21 UT and 15:11 UT in the duskside region and at 15:11 UT in the dawnside region.
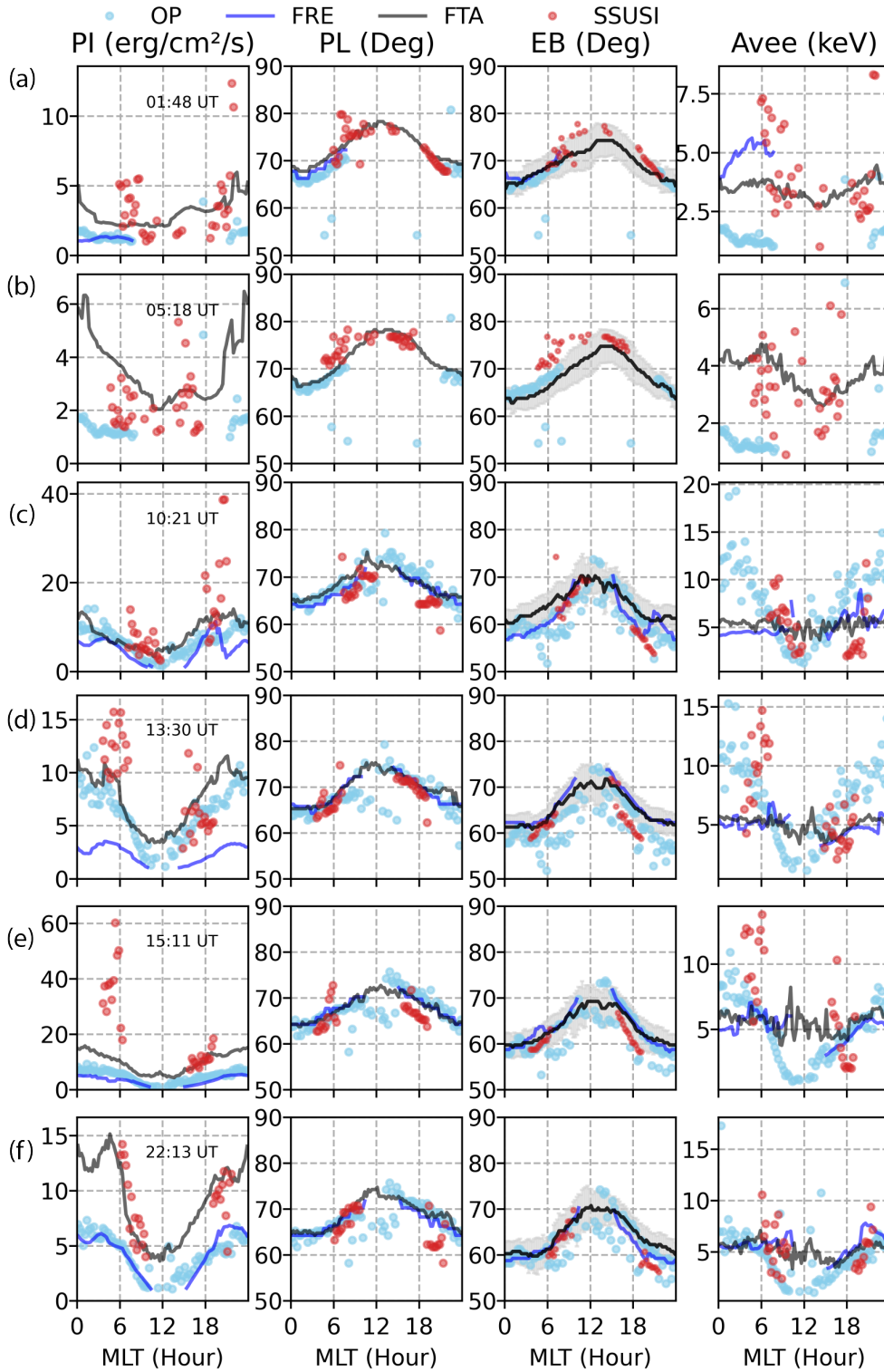
Figure 13 shows the peak intensity (first column) as a function of MLT for the three models and the SSUSI measurements. The peak intensity by SSUSI was larger than model predictions generally and exceeded 20 $erg\ cm^{-2}\ s^{-1}$ at higher activity levels. It seems difficult for models to realistically capture intense aurora. Relatively, the FTA model specified higher energy flux and was consistent with some peaks in the measurements, especially at 22:13 UT. This can be partially explained by the AE index organizing the FTA model so that it more closely controlled the auroral patterns directly. In the second and third columns, the EB and the peak intensity locations in each MLT sector are compared. The three models and the measurements were relatively consistent on the dawnside. On the duskside, the three models put the peak intensity location at too high of latitude at 15:11 UT and 22:13 UT. In terms of the EB, the observations were at lower latitudes than the predictions, but the FRE and OP models were closer to SSUSI measurements at 10:21 UT and 22:13 UT.
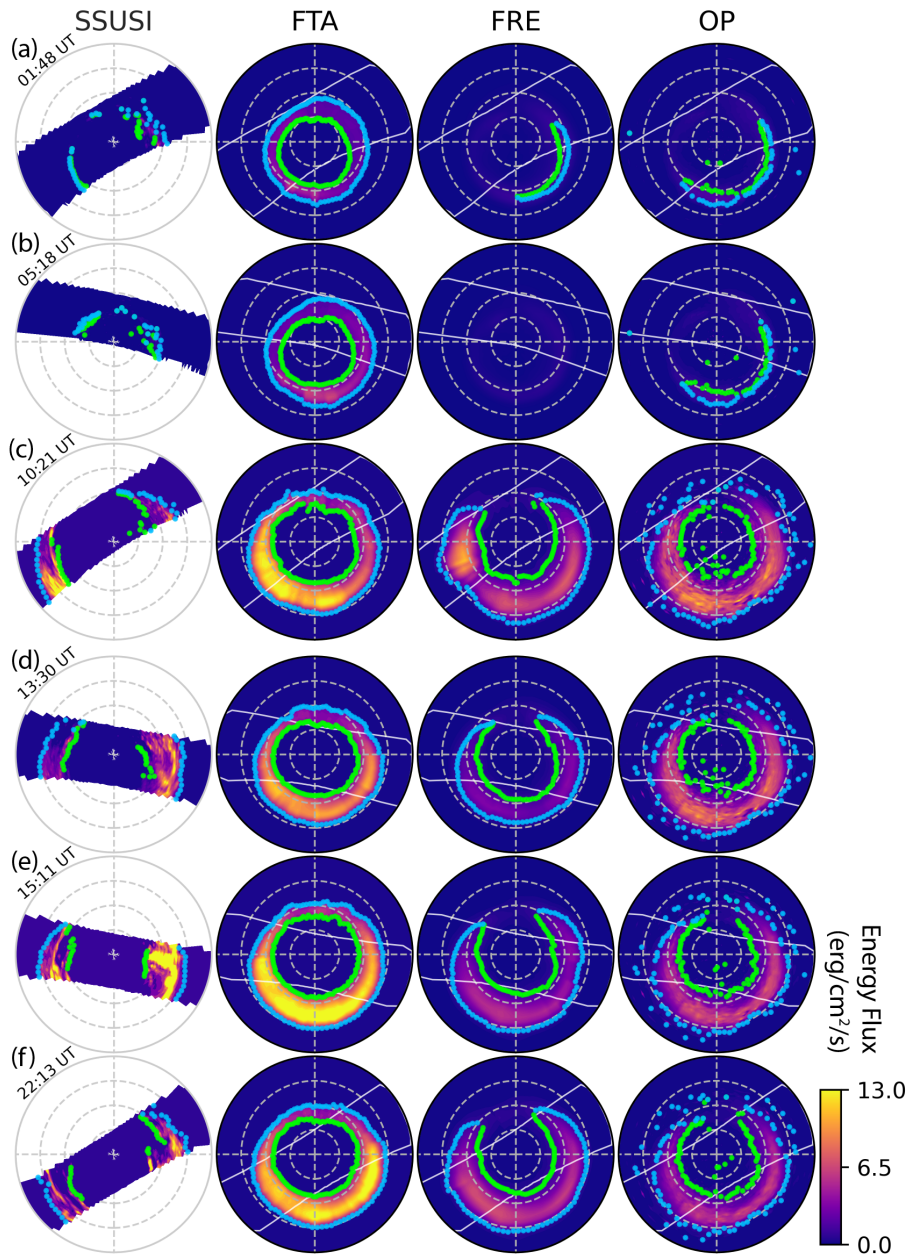
Figure 11. Comparisons of the SSUSI measurements and the predictions of the three models (energy flux > 0). From the left to the right, the four columns represent the energy flux from SSUSI, the FTA model, the FRE model, and the OP model. The bright blue and green dots represent the 1.0 $erg\ cm^{-2}\ s^{-1}$ locations in the measurements and models. The cutoff of the field view of SSUSI was superimposed on the predictions. All the dial plots are in MLat and MLT coordinates with noon (1200 MLT) at the top and dusk (1800 MLT) at the left. The MLat range is from 50° to 90° and the white dashed circles represent MLat at 80°, 70°, and 60°.
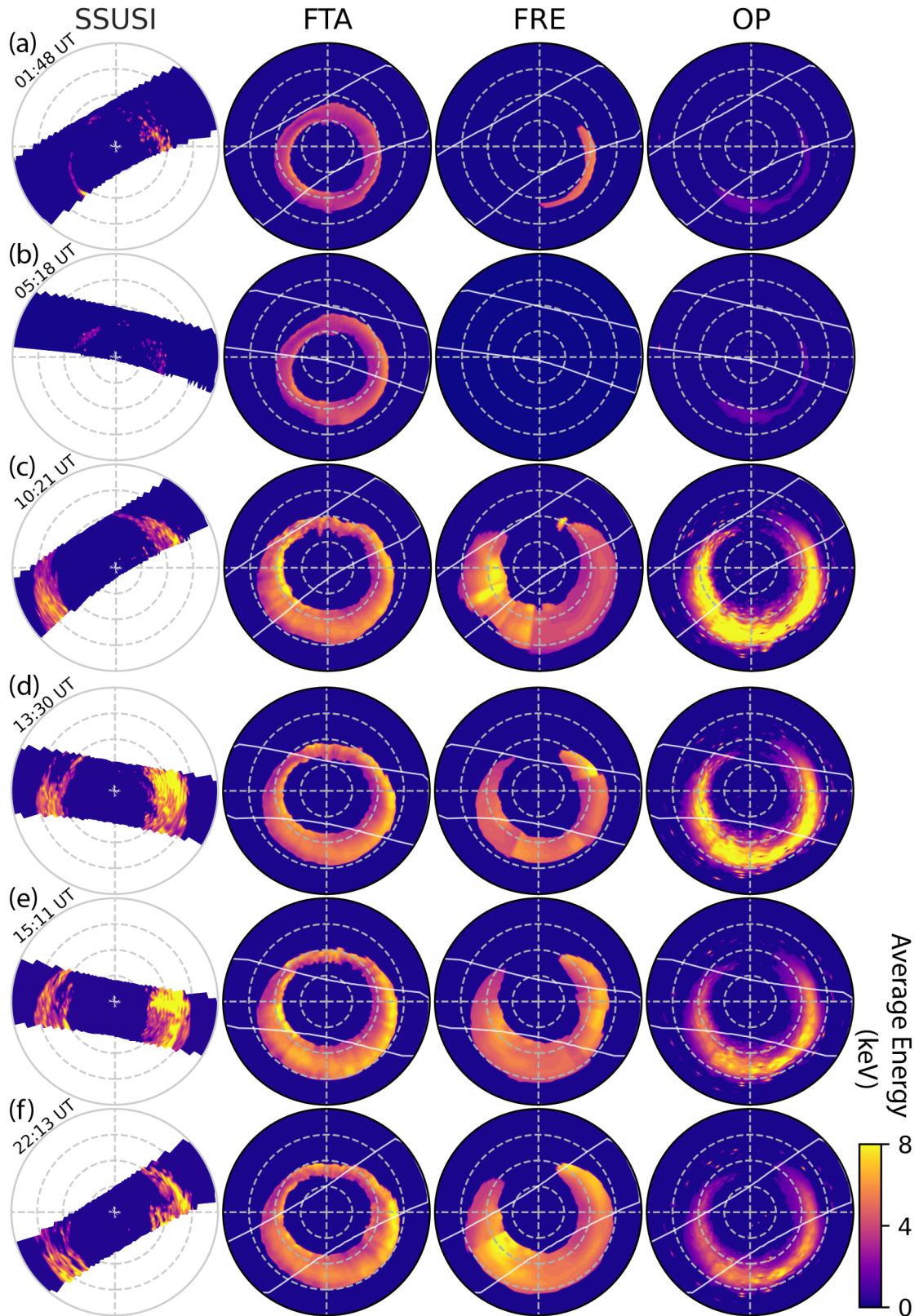
Figure 12. Similar to Figure 11, but for the average energy. The average energy is only shown if the energy flux is larger than 1.0 $erg\ cm^{-2}\ s^{-1}$.

Figure 13. The peak intensity (first column), the peak intensity location (second column), the EB (third column), and the average energy at the peak intensity location (fourth column) as a function of the MLT for the SSUSI measurements and the models. The 6 orbits are the same as those in Figures 11 and 12.

For all the 38 orbits of DMSP on 17 March 2013, when AE was lower than 900 nT, the differences of the peak intensity, the EB, and the peak intensity location for each MLT bin between the models and the measurements were calculated. The distributions of the differences are shown in Figure 14. For each orbit, only if all three models had predictions, the data were included. Since the DMSP satellites flew mostly in the dawn-dusk direction, the distribution was calculated separately for the dawnside (0000-1200 MLT) and the duskside (1200-2400 MLT). The FTA model showed the lowest difference median in the peak intensity for each MLT bin, especially on the duskside. The locations of the peak intensity and the EB, were similar for the three models statistically given the latitudinal resolution was 0.5°, but the OP model had a relatively smaller median and a larger uncertainty on the duskside for the EB. At dawn, all models were almost unbiased in the locations of the peak intensity and EB, while at dusk the models were about 3°-5.5° poleward in both the EB and peak intensity location.

Figure 12 shows that at lower activity levels, the OP model specified very low average energy, while the FTA and the FRE models had higher energy if there were auroral emissions. For higher activity, the average energy of the OP model varied more in magnitude and tended to have larger values on the nightside overall, while the enhanced regions in FRE and FTA models were on the equatorward edge on the morning side and at higher latitudes on the duskside. In Figure 13, for the 6 orbits, the average energy (the fourth column) at the location of the peak of the energy flux for each MLT bin is shown. For the two times at lower activity levels, the average energy of the OP model was lower than the observations and other model predictions. At higher activity times, the FTA model predicted the average energy of approximate 5 keV, consistent with the FRE model. The OP model predicted higher average energy on the nightside, which decreased toward noon. This matched the SSUSI data better on the nightside than the other models. For all 38 orbits, the distribution of the differences in the average energy between the models and the measurements is shown in the fourth column in Figure 14. Statistically, the models estimated the average energy better on the dawnside and overestimated it on the duskside. The average energy from the FRE and FTA models were similar to a great degree, doing slightly better than the OP model by about 1 keV.
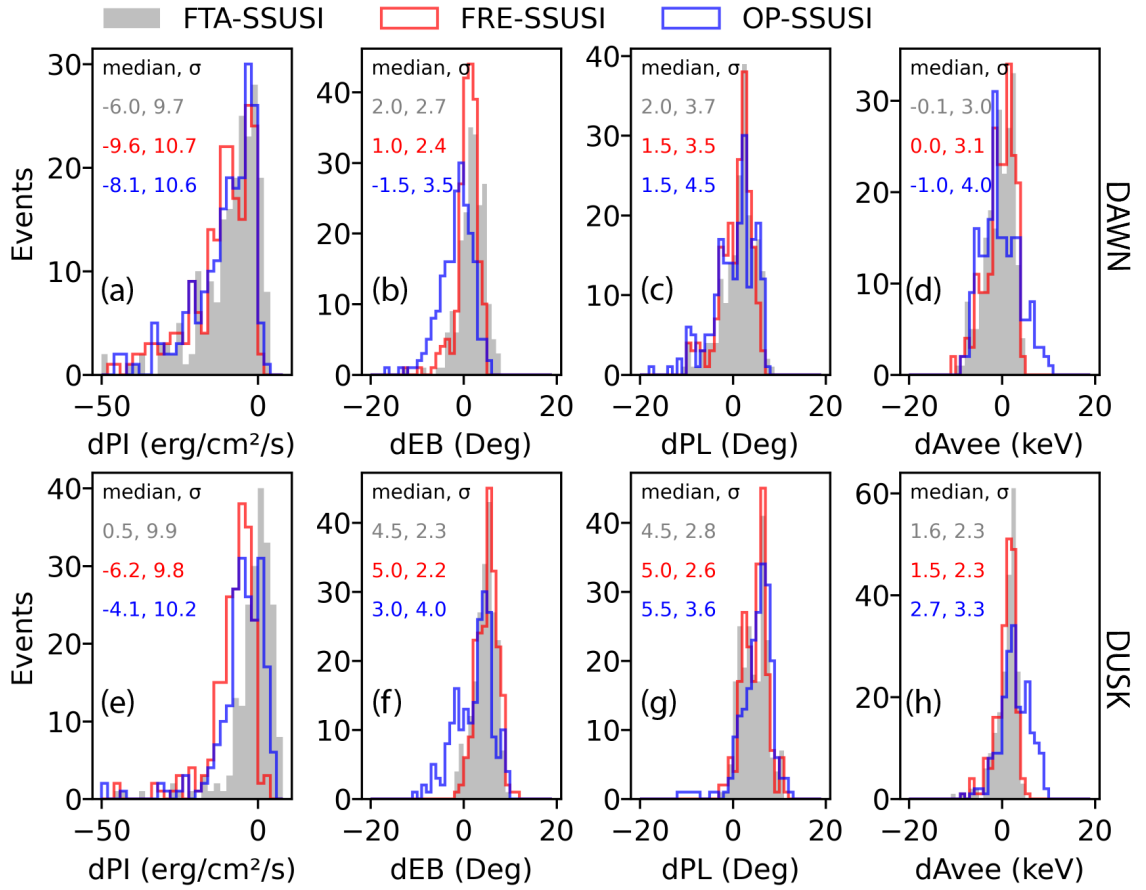
Figure 14. The distributions of the differences of the peak intensity (first column), the peak intensity location (second column), the EB (third column), and the average energy at the peak intensity location (fourth column), between the three models and the SSUSI measurements. The first and the second rows are for dawnside (0000-1200 MLT) and duskside (1200-2400 MLT), respectively. The grey, the red, and the blue bars represent FTA-SSUSI, FRE-SSUSI, OP-SSUSI, respectively. The median and one standard deviation (σ) for each parameter were denoted.

5.4 Auroral Power (AP) Comparison

The APs of the measured and modeled aurora in the region observed by SSUSI were calculated and the correlation coefficients between the measurements and the predictions were compared. Given that the comparisons were limited to periods with AE no larger than 900 nT, as mentioned above, there were situations where some MLT regions were excluded in the individual auroral image of SSUSI, under which we denoted the AP of this auroral image as "partially covered". Conversely, if the entire swath was used, the AP was denoted as "fully covered". In Figure 15, the coefficients between the SSUSI measurements and the FRE, OP, and FTA models were 0.76, 0.82, and 0.81, respectively. Linear least-squares fittings were also performed and the slopes of the fitted lines for the FRE, OP, and FTA models were 0.31, 0.39, and 0.56, respectively. When the measured AP was lower than about 20 GW, the FRE and OP models predicted the AP better than the FTA model, though most of the time they underestimated the AP, while the FTA model overestimated it. This is because during lower activity, when the aurora was very weak, like in Figures 11a and 11b, the FTA model predicted the intense region but the size of the dim region was overestimated, while the FRE and OP models underestimated both, resulting in a better prediction of the integrated energy flux (for low activity). As can be seen in Figure 11, the FTA model's width from dawn to noon on the dayside was large for low activity. While there was relatively weak aurora in this region, it was broad, providing too large of an AP for low activity levels. However, as geomagnetic activity increased with SSUSI AP > 20 GW, the results of FRE and OP models deviated from SSUSI measurements more due to their underestimation, whereas the results of the FTA model were relatively close to the measurements. Figure 15 shows that the model predictions seemed to deteriorate more for all of the models when the total energies were high enough (SSUSI AP > 50 GW), although the FTA model was closest to the measurements at these higher levels of activity.

6 Summary

A new auroral electron precipitation model, the FTA model, was constructed using cumulative energy bins instead of latitude bins, based on the Polar UVI N_2 LBHl and LBHs emission data from 1 January 1997 to 30 June 1998, and parameterized by the AE index. A summary of the findings of this model and study are as follows:

–34–
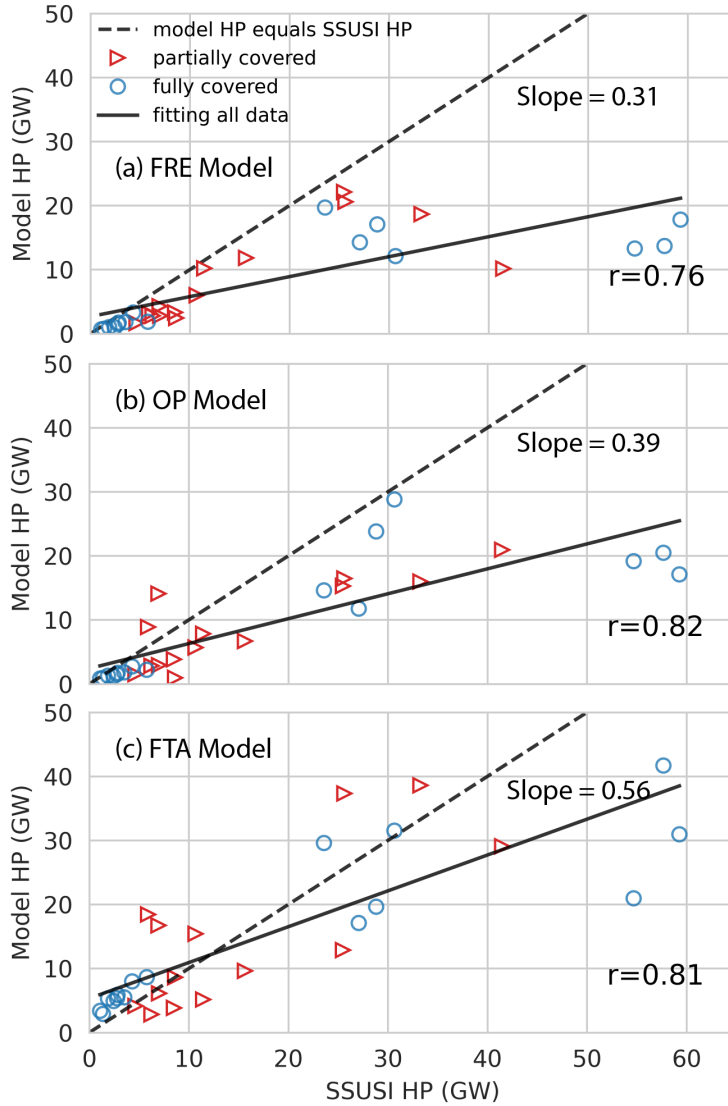
Figure 15. Correlation coefficients between the measurements and the FRE (a), OP (b), and FTA (c) models. The solid line represents the linear fitting between the observation and the prediction, while the dashed is the linear line with the data and model being equal, serving as a comparison with the former.

1. Compared with traditional MLT/MLat models, the FTA model specified narrower patterns of the energy flux with different dawn-dusk asymmetries and fine structures as geomagnetic activity increases. The behavior of the auroral patterns seems to indicate different levels of driving causing the aurora to behave differently, with the aurora during lower activity times indicating possible characteristics of individual substorms with the peak in auroral brightness occurring pre-midnight; while medium levels of driving show the peak in the aurora moving to the midnight and post-midnight sectors; and finally intense driving indicates general strong auroral activity everywhere. Further work is needed to determine the dependencies of the aurora on different drivers, which may be able to be parameterized by AU, AL, and Dst.

2. The auroral boundaries and the peak intensity were investigated statistically. As AE increases, the equatorward boundary moves to lower latitudes everywhere, while the poleward boundary moves poleward in the 2300-0300 MLT region and equatorward in other MLT sectors. Combined, this means that the aurora widens on the nightside and narrows on the dayside with increasing activity. The peak intensity for each MLT bin increases almost linearly with AE. The change rate of intensity with AE has a diurnal pattern, with the peak on the nightside and the trough at noon. At lower activity levels, the maximum of the peaks occurs pre-midnight, but switches to post-midnight at around 500 nT.

3. Predictions from the FRE, OP, and FTA models were compared with measurements by SSUSI on 17 March 2013. Among the three models, the FTA model had the most confined pattern with the highest energy flux, agreeing with the spatial and temporal evolution of SSUSI measurements better with an improvement of the peak intensity especially on the duskside statistically. The EB and peak intensity locations of the three models were more consistent with SSUSI on the dawnside but were too poleward on the duskside. The FTA and FRE models specified very similar average energy differences with the SSUSI measurements, doing slightly better by ~1 keV than the OP model. While the correlation coefficients between the AP measurements and the model results were very similar, the FRE model had the lowest slope (slope=0.31), under-predicting the AP significantly at higher activities, while the OP model still under-predicted the AP (slope=0.39), but was higher than the FRE model. Finally, the FTA model

over-predicted the AP for weak driving (SSUSI AP < 20 GW), and under-predicted it for strong driving, but was still larger than the other two models (slope=0.56), and closest to the actual measured AP.

Since the global imagers focused on the northern hemisphere, the new precipitation model did not contain the southern hemisphere. To address this limitation, we are working on extending this model to include tilt-angle effects and incorporating the measurements by multiple SSUSIs to calculate independent models for the northern and southern hemispheres.

References

Akasofu, S.-I. (1966). The auroral oval, the auroral substorm, and their relations with the internal structure of the magnetosphere. *Planetary and Space Science*, *14*(7), 587 - 595. Retrieved from `http://www.sciencedirect.com/science/article/pii/0032063366900432` doi: https://doi.org/10.1016/0032-0633(66)90043-2

Baker, J. B., Clauer, C. R., Ridley, A. J., Papitashvili, V. O., Brittnacher, M. J., & Newell, P. T. (2000). The nightside poleward boundary of the auroral oval as seen

by dmsp and the ultraviolet imager. *Journal of Geophysical Research: Space Physics*, *105*(A9), 21267-21280. Retrieved from https://agupubs.onlinelibrary.wiley.com/doi/abs/10.1029/1999JA000363 doi: 10.1029/1999JA000363

Borovsky, J. E., Suszcynsky, D. M., Buchwald, M. I., & DeHaven, H. V. (1991). Measuring the thicknesses of auroral curtains. *Arctic*, 231–238.

Brautigam, D., Gussenhoven, M., & Hardy, D. A. (1991). A statistical study on the effects of imf bz and solar wind speed on auroral ion and electron precipitation. *Journal of Geophysical Research: Space Physics*, *96*(A4), 5525–5538.

Brittnacher, M., Elsen, R., Parks, G., Chen, L., Germany, G., & Spann, J. (1997, January). A dayside auroral energy deposition case study using the Polar Ultraviolet Imager. *Geophysical Research Letters*, *24*(8), 991-994. doi: 10.1029/97GL00257

Brittnacher, M., Fillingim, M., Parks, G., Germany, G., & Spann, J. (1999, June). Polar cap area and boundary motion during substorms. *Journal of Geophysical Research*, *104*(A6), 12251-12262. doi: 10.1029/1998JA900097

Cai, X., & Clauer, C. R. (2013, October). Magnetospheric sawtooth events during the solar cycle 23. *Journal of Geophysical Research (Space Physics)*, *118*(10), 6378-6388. doi: 10.1002/2013JA018819

Carbary, J. F. (2005, October). A Kp-based model of auroral boundaries. *Space Weather*, *3*(10), S10001. doi: 10.1029/2005SW000162

Carbary, J. F., Sotirelis, T., Newell, P. T., & Meng, C. I. (2003, January). Auroral boundary correlations between UVI and DMSP. *Journal of Geophysical Research (Space Physics)*, *108*(A1), 1018. doi: 10.1029/2002JA009378

Carter, J. A., Milan, S. E., Coxon, J. C., Walach, M.-T., & Anderson, B. J. (2016). Average field-aligned current configuration parameterized by solar wind conditions. *Journal of Geophysical Research: Space Physics*, *121*(2), 1294-1307. Retrieved from https://agupubs.onlinelibrary.wiley.com/doi/abs/10.1002/2015JA021567 doi: 10.1002/2015JA021567

Chisham, G. (2017). A new methodology for the development of high-latitude ionospheric climatologies and empirical models. *Journal of Geophysical Research: Space Physics*, *122*(1), 932-947. Retrieved from https://agupubs.onlinelibrary.wiley.com/doi/abs/10.1002/2016JA023235

doi: https://doi.org/10.1002/2016JA023235

DeJong, A., Bell, J. M., & Ridley, A. (2018). Comparison of the ionosphere during an smc initiating substorm and an isolated substorm. *Journal of Geophysical Research: Space Physics*, *123*(6), 4939–4951.

DeJong, A. D., Ridley, A. J., Cai, X., & Clauer, C. R. (2009, August). A statistical study of BRIs (SMCs), isolated substorms, and individual sawtooth injections. *Journal of Geophysical Research (Space Physics)*, *114*(A8), A08215. doi: 10.1029/2008JA013870

Ding, G.-X., He, F., Zhang, X.-X., & Chen, B. (2017, February). A new auroral boundary determination algorithm based on observations from TIMED/GUVI and DMSP/SSUSI. *Journal of Geophysical Research (Space Physics)*, *122*(2), 2162-2173. doi: 10.1002/2016JA023295

Elphic, R. C., Bonnell, J. W., Strangeway, R. J., Kepko, L., Ergun, R. E., McFadden, J. P., . . . Pfaff, R. (1998, January). The auroral current circuit and field-aligned currents observed by FAST. *Geophysical Research Letters*, *25*(12), 2033-2036. doi: 10.1029/98GL01158

Emery, B. A., Evans, D. S., Greer, M. S., Holeman, E., Kadinsky-Cade, K., Rich, F. J., & Xu, W. (2006). The low energy auroral electron and ion hemispheric power after noaa and dmsp intersatellite adjustments. *Tech. Note NCAR/TN-470+ STR*.

Feldstein, Y. I. (1973). Auroral oval. *Journal of Geophysical Research (1896-1977)*, *78*(7), 1210-1213. Retrieved from `https://agupubs.onlinelibrary.wiley.com/doi/abs/10.1029/JA078i007p01210` doi: 10.1029/JA078i007p01210

Forsyth, C., Sergeev, V. A., Henderson, M. G., Nishimura, Y., & Gallardo-Lacourt, B. (2020, April). Physical Processes of Meso-Scale, Dynamic Auroral Forms. *Space Sci Rev*, *216*(4), 46. doi: 10.1007/s11214-020-00665-y

Frank, L. A., & Craven, J. D. (1988). Imaging results from dynamics explorer 1. *Reviews of Geophysics*, *26*(2), 249-283. Retrieved from `https://agupubs.onlinelibrary.wiley.com/doi/abs/10.1029/RG026i002p00249` doi: 10.1029/RG026i002p00249

Frey, H. U. (2007). Localized aurora beyond the auroral oval. *Reviews of Geophysics*, *45*(1).

Frey, H. U., Mende, S. B., Angelopoulos, V., & Donovan, E. F. (2004, October). Substorm onset observations by IMAGE-FUV. *Journal of Geophysical Research*

(Space Physics), *109*(A10), A10304. doi: 10.1029/2004JA010607

Fuller-Rowell, T. J., & Evans, D. S. (1987, July). Height-integrated Pedersen and Hall conductivity patterns inferred from the TIROS-NOAA satellite data. *Journal of Geophysical Research*, *92*(A7), 7606-7618. doi: 10.1029/JA092iA07p07606

Germany, G. A., Parks, G. K., Ranganath, H., Elsen, R., Richards, P. G., Swift, W., . . . Brittnacher, M. (1998). Analysis of auroral morphology: Substorm precursor and onset on january 10, 1997. *Geophysical Research Letters*, *25*(15), 3043-3046. Retrieved from https://agupubs.onlinelibrary.wiley.com/doi/abs/10.1029/98GL01220 doi: 10.1029/98GL01220

Germany, G. A., Torr, D. G., Richards, P. G., Torr, M. R., & John, S. (1994, December). Determination of ionospheric conductivities from FUV auroral emissions. *Journal of Geophysical Research*, *99*(A12), 23297-23306. doi: 10.1029/94JA02038

Hardy, D. A., Gussenhoven, M. S., & Holeman, E. (1985, May). A statistical model of auroral electron precipitation. *Journal of Geophysical Research*, *90*(A5), 4229-4248. doi: 10.1029/JA090iA05p04229

Hartigan, J. A., & Wong, M. A. (1979). Algorithm as 136: A k-means clustering algorithm. *Journal of the royal statistical society. series c (applied statistics)*, *28*(1), 100–108.

Henderson, M. G. (2004, June). The May 2-3, 1986 CDAW-9C interval: A sawtooth event. *Geophysical Research Letters*, *31*(11), L11804. doi: 10.1029/2004GL019941

Heppner, J., & Maynard, N. (1987). Empirical high-latitude electric field models. *J. Geophys. Res.*, *92*, 4467.

Kauristie, K., Weygand, J., Pulkkinen, T. I., Murphree, J. S., & Newell, P. T. (1999, February). Size of the auroral oval: UV ovals and precipitation boundaries compared. *Journal of Geophysical Research*, *104*(A2), 2321-2332. doi: 10.1029/1998JA900046

Kilcommons, L. M., Redmon, R. J., & Knipp, D. J. (2017, August). A new DMSP magnetometer and auroral boundary data set and estimates of field-aligned currents in dynamic auroral boundary coordinates. *Journal of Geophysical Research (Space Physics)*, *122*(8), 9068-9079. doi: 10.1002/2016JA023342

Korth, H., Anderson, B. J., Frey, H. U., Immel, T. J., & Mende, S. B. (2004). Conditions governing localized high-latitude dayside aurora. *Geophysical Research Letters*,

31(4). Retrieved from

https://agupubs.onlinelibrary.wiley.com/doi/abs/10.1029/2003GL018911

doi: 10.1029/2003GL018911

Korth, H., Zhang, Y., Anderson, B. J., Sotirelis, T., & Waters, C. L. (2014, August).
Statistical relationship between large-scale upward field-aligned currents and
electron precipitation. *Journal of Geophysical Research (Space Physics)*, *119*(8),
6715-6731. doi: 10.1002/2014JA019961

Landry, R. G., & Anderson, P. C. (2018). An auroral boundary-oriented model of
subauroral polarization streams (saps). *Journal of Geophysical Research: Space
Physics*, *123*(4), 3154-3169. Retrieved from
https://agupubs.onlinelibrary.wiley.com/doi/abs/10.1002/2017JA024921
doi: https://doi.org/10.1002/2017JA024921

Liou, K., Newell, P. T., Meng, C. I., Brittnacher, M., & Parks, G. (1997, December).
Synoptic auroral distribution: A survey using Polar ultraviolet imagery. *Journal of
Geophysical Research*, *102*(A12), 27197-27206. doi: 10.1029/97JA02638

Liou, K., Newell, P. T., Sibeck, D. G., Meng, C. I., Brittnacher, M., & Parks, G. (2001,
April). Observation of IMF and seasonal effects in the location of auroral substorm
onset. *Journal of Geophysical Research*, *106*(A4), 5799-5810. doi:
10.1029/2000JA003001

Luan, X., Zhou, S., & Dou, X. (2018, May). Auroral Energy Flux Distribution Over the
Nightside Auroral Oval Observed by the DMSP F16/SSUSI: Seasonal, Geomagnetic,
and Solar Activity Dependences. *Journal of Geophysical Research (Space Physics)*,
123(5), 4457-4466. doi: 10.1029/2017JA023970

Lui, A. T. Y., Venkatesan, D., & Murphree, J. S. (1989, May). Auroral bright spots on
the dayside oval. *Journal of Geophysical Research*, *94*(A5), 5515-5522. doi:
10.1029/JA094iA05p05515

Maggs, J. E., & Davis, T. N. (1968, February). Measurements of the thicknesses of
auroral structures. *Planetary and Space Science*, *16*(2), 205,IN1,207-206,IN2,209.
doi: 10.1016/0032-0633(68)90069-X

Mende, S. B. (2016, October). Observing the magnetosphere through global auroral
imaging: 2. Observing techniques. *Journal of Geophysical Research (Space Physics)*,
121(10), 10,638-10,660. doi: 10.1002/2016JA022607

Milan, S. E. (2009). Both solar wind-magnetosphere coupling and ring current intensity

825   control of the size of the auroral oval. *Geophysical Research Letters*, *36*(18).

826   Retrieved from

827   `https://agupubs.onlinelibrary.wiley.com/doi/abs/10.1029/2009GL039997`

828   doi: 10.1029/2009GL039997

829   Milan, S. E., Hutchinson, J., Boakes, P. D., & Hubert, B. (2009, July). Influences on the

830   radius of the auroral oval. *Annales Geophysicae*, *27*(7), 2913-2924. doi:

831   10.5194/angeo-27-2913-2009

832   Mitchell, E. J., Newell, P. T., Gjerloev, J. W., & Liou, K. (2013). Ovation-sm: A model

833   of auroral precipitation based on supermag generalized auroral electrojet and

834   substorm onset times. *Journal of Geophysical Research: Space Physics*, *118*(6),

835   3747-3759. Retrieved from

836   `https://agupubs.onlinelibrary.wiley.com/doi/abs/10.1002/jgra.50343` doi:

837   10.1002/jgra.50343

838   Mooney, M. K., Forsyth, C., Rae, I. J., Chisham, G., Coxon, J. C., Marsh, M. S., . . .

839   Hubert, B. (2020, April). Examining Local Time Variations in the Gains and Losses

840   of Open Magnetic Flux During Substorms. *Journal of Geophysical Research (Space*

841   *Physics)*, *125*(4), e27369. doi: 10.1029/2019JA027369

842   Murphy, K. R., Mann, I. R., Rae, I. J., Waters, C. L., Frey, H. U., Kale, A., . . . Korth, H.

843   (2013). The detailed spatial structure of field-aligned currents comprising the

844   substorm current wedge. *Journal of Geophysical Research: Space Physics*, *118*(12),

845   7714-7727. Retrieved from

846   `https://agupubs.onlinelibrary.wiley.com/doi/abs/10.1002/2013JA018979`

847   doi: 10.1002/2013JA018979

848   Newell, P. T., Liou, K., Zhang, Y., Sotirelis, T., Paxton, L. J., & Mitchell, E. J. (2014,

849   June). OVATION Prime-2013: Extension of auroral precipitation model to higher

850   disturbance levels. *Space Weather*, *12*(6), 368-379. doi: 10.1002/2014SW001056

851   Newell, P. T., Liou, K., Zhang, Y., Sotirelis, T. S., Paxton, L. J., & Mitchell, E. J. (2015).

852   Auroral precipitation models and space weather. In *Auroral dynamics and space*

853   *weather* (p. 275-290). American Geophysical Union (AGU). Retrieved from

854   `https://agupubs.onlinelibrary.wiley.com/doi/abs/10.1002/`

855   `9781118978719.ch18` doi: 10.1002/9781118978719.ch18

856   Newell, P. T., Sotirelis, T., Liou, K., Lee, A. R., Wing, S., Green, J., & Redmon, R.

857   (2010b). Predictive ability of four auroral precipitation models as evaluated using

polar uvi global images. *Space Weather*, *8*(12). Retrieved from

https://agupubs.onlinelibrary.wiley.com/doi/abs/10.1029/2010SW000604

doi: 10.1029/2010SW000604

Newell, P. T., Sotirelis, T., Liou, K., Meng, C. I., & Rich, F. J. (2007, January). A nearly
universal solar wind-magnetosphere coupling function inferred from 10
magnetospheric state variables. *Journal of Geophysical Research (Space Physics)*,
112(A1), A01206. doi: 10.1029/2006JA012015

Newell, P. T., Sotirelis, T., & Wing, S. (2009, September). Diffuse, monoenergetic, and
broadband aurora: The global precipitation budget. *Journal of Geophysical
Research (Space Physics)*, *114*(A9), A09207. doi: 10.1029/2009JA014326

Newell, P. T., Sotirelis, T., & Wing, S. (2010a, March). Seasonal variations in diffuse,
monoenergetic, and broadband aurora. *Journal of Geophysical Research (Space
Physics)*, *115*(A3), A03216. doi: 10.1029/2009JA014805

Nishimura, Y., Lessard, M. R., Katoh, Y., Miyoshi, Y., Grono, E., Partamies, N., . . .
Kurita, S. (2020, January). Diffuse and Pulsating Aurora. *Space Science Reviews*,
216(1), 4. doi: 10.1007/s11214-019-0629-3

Paschmann, G., Haaland, S., & Treumann, R. (2012). *Auroral plasma physics* (Vol. 15).
Springer Science & Business Media. (pages:21-39)

Paxton, L. J., & Meng, C.-I. (1999). Auroral imaging and space-based optical remote
sensing. *Johns Hopkins APL technical digest*, *20*(4), 556–569.

Paxton, L. J., Meng, C.-I., Fountain, G. H., Ogorzalek, B. S., Darlington, E. H., Gary,
S. A., . . . Smith, B. E. (1992, June). Special sensor ultraviolet spectrographic
imager: an instrument description. In S. Chakrabarti & A. B. Christensen (Eds.),
Instrumentation for planetary and terrestrial atmospheric remote sensing (Vol. 1745,
p. 2-15). doi: 10.1117/12.60595

Paxton, L. J., Meng, C.-I., Fountain, G. H., Ogorzalek, B. S., Darlington, E. H., Gary,
S. A., . . . Jr., R. E. D. (1993). SSUSI: horizon-to-horizon and limb-viewing
spectrographic imager for remote sensing of environmental parameters. In
R. E. Huffman (Ed.), *Ultraviolet technology iv* (Vol. 1764, pp. 161 – 176). SPIE.
Retrieved from https://doi.org/10.1117/12.140846 doi: 10.1117/12.140846

Paxton, L. J., Schaefer, R. K., Zhang, Y., & Kil, H. (2017, February). Far ultraviolet
instrument technology. *Journal of Geophysical Research (Space Physics)*, *122*(2),
2706-2733. doi: 10.1002/2016JA023578

Pytte, T., McPherron, R. L., Hones, J., E. W., & West, J., H. I. (1978, February). Multiple-satellite studies of magnetospheric substorms: Distinction between polar magnetic substorms and convection-driven negative bays. *Journal of Geophysical Research*, *83*(A2), 663-679. doi: 10.1029/JA083iA02p00663

Redmon, R. J., Peterson, W. K., Andersson, L., Kihn, E. A., Denig, W. F., Hairston, M., & Coley, R. (2010). Vertical thermal o+ flows at 850 km in dynamic auroral boundary coordinates. *Journal of Geophysical Research: Space Physics*, *115*(A11). Retrieved from
https://agupubs.onlinelibrary.wiley.com/doi/abs/10.1029/2010JA015589
doi: https://doi.org/10.1029/2010JA015589

Rich, F., & Hairston, M. (1994). Large-scale convection patterns observed by DMSP. *J. Geophys. Res.*, *99*, 3827-3844.

Rostoker, G. (1991, April). A quantitative relationship between AE and Kp. *J. Geophys. Res.*, *96*(A4), 5853-5857. doi: 10.1029/90JA02752

Sandahl, I., Sergienko, T., & Brändström, U. (2008, December). Fine structure of optical aurora. *Journal of Atmospheric and Solar-Terrestrial Physics*, *70*(18), 2275-2292. doi: 10.1016/j.jastp.2008.08.016

Sotirelis, T., & Newell, P. T. (2000). Boundary-oriented electron precipitation model. *Journal of Geophysical Research: Space Physics*, *105*(A8), 18655-18673. Retrieved from
https://agupubs.onlinelibrary.wiley.com/doi/abs/10.1029/1999JA000269
doi: 10.1029/1999JA000269

Strickland, D. J., Jasperse, J. R., & Whallen, J. A. (1983, October). Dependence of auroral FUV emissions on the incident electron spectrum and neutral atmosphere. *Journal of Geophysical Research*, *88*(A10), 8051-8062. doi: 10.1029/JA088iA10p08051

Torr, M. R., Torr, D. G., Zukic, M., Johnson, R. B., Ajello, J., Banks, P., . . . Spann, J. (1995, February). A Far Ultraviolet Imager for the International Solar-Terrestrial Physics Mission. *Space Science Reviews*, *71*(1-4), 329-383. doi: 10.1007/BF00751335

Walach, M. T., Milan, S. E., Murphy, K. R., Carter, J. A., Hubert, B. A., & Grocott, A. (2017, June). Comparative study of large-scale auroral signatures of substorms, steady magnetospheric convection events, and sawtooth events. *Journal of*

924   *Geophysical Research (Space Physics)*, *122*(6), 6357-6373. doi:

925   10.1002/2017JA023991

926 Wang, Q., Meng, Q., Hu, Z., Xing, Z., Liang, J., & Hu, H. (2011). Extraction of auroral

927   oval boundaries from uvi images: A new flicm clustering-based method and its

928   evaluation. *Advances in Polar Science*, *22*(3-English), 184-191.

929 Weimer, D. R. (2005). Improved ionospheric electrodynamic models and application to

930   calculating joule heating rates. *J. Geophys. Res.*, *110*, 05306. doi:

931   10.1029/2004JA010884

932 Zhang, Y., & Paxton, L. (2008). An empirical kp-dependent global auroral model based

933   on timed/guvi fuv data. *Journal of Atmospheric and Solar-Terrestrial Physics*,

934   *70*(8), 1231 - 1242. Retrieved from

935   `http://www.sciencedirect.com/science/article/pii/S1364682608000758` doi:

936   https://doi.org/10.1016/j.jastp.2008.03.008

937 Zhu, Q., Deng, Y., Richmond, A., Maute, A., Chen, Y.-J., Hairston, M., . . . Mitchell, E.

938   (2020, January). Impacts of Binning Methods on High-Latitude Electrodynamic

939   Forcing: Static Versus Boundary-Oriented Binning Methods. *Journal of Geophysical

940   Research (Space Physics)*, *125*(1), e27270. doi: 10.1029/2019JA027270